Heliyon 10 (2024) e34348

Contents lists available at ScienceDirect

Heliyon

journal homepage: www.cell.com/heliyon

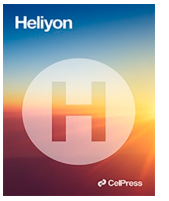

Research article

Immune infiltration analysis based on pyroptosis-related gene in metabolic dysfunction-associated fatty liver disease

Xin Lian, Xulei Tang *

The First Clinical Medical College of Lanzhou University, Lanzhou, Gansu, 730000, China

ARTICLE INFO

Keywords:
Metabolic dysfunction-associated fatty liver disease
Pyroptosis-related gene
Immune infiltration
Bioinformatics

ABSTRACT

Introduction: Metabolic dysfunction-associated fatty liver disease (MAFLD) is a prevalent chronic disease that can involve pyroptosis. The primary objective of this study was to conduct a thorough and comprehensive analysis the pyroptosis-related genes in MAFLD.
Methods: We identified pyroptosis-related differentially expressed genes (PRDEGs) in both healthy individuals and MAFLD patients. Using various bioinformatic approaches, we conducted an immune infiltration analysis from multiple perspectives.
Results: A total of 20 pyroptosis-related LASSO genes were obtained, and 10 hub genes were used to do immune infiltration analysis. The hub genes were utilized in the construction of interaction networks between mRNA-miRNA and mRNA-TF. Immune characteristics analysis revealed multiple immune cell types significantly related to PRDEG expression, particularly genes HSP90AA1, TSLP, CDK9, and BRD4.
Conclusion: Pyroptosis-related immune infiltration might be a mechanism of MAFLD progression and offers a research direction for potential treatment techniques.

1. Introduction

Metabolic dysfunction-associated fatty liver disease (MAFLD), formerly referred to as non-alcoholic fatty liver disease (NAFLD), stems from profound metabolic dysregulation linked to the pernicious trio of obesity, type 2 diabetes, and a constellation of other metabolic risk factors [1]. MAFLD is a prevalent chronic disease, with a significant impact on more than a quarter of the global population [2]. Despite the preponderance of individuals afflicted with MAFLD residing in the hepatic steatosis phase, a select few unfortunately exhibit inflammatory injury, a condition that has the potential to emerge at any given juncture. This injury, though infrequent, is of significant concern as it can herald the progression of the disease towards more severe manifestations [3]. Among those diagnosed with steatohepatitis, the rate of fibrosis progression varies significantly, with some individuals experiencing rapid fibrosis while others progress more slowly [4]. The pathogenesis of steatohepatitis and liver cirrhosis is primarily driven by inflammatory infiltrates and hepatocyte damage, which are associated with specific immune cell populations [5]. Various studies have linked steatohepatitis to particular immunological profiles in liver [6,7] Moreover, the occurrence of hepatocyte pyroptosis has the potential to trigger the development of steatohepatitis, thereby accelerating the deterioration of fatty liver conditions. Despite the significant strides in understanding MAFLD, the precise mechanisms underlying its pathogenesis remain elusive. Current treatment options are limited, with weight loss and exercise being the primary strategies. The quest to identify effective preventive and therapeutic

* Corresponding author.
E-mail address: xulei_tang@126.com (X. Tang).

https://doi.org/10.1016/j.heliyon.2024.e34348
Received 9 October 2023; Received in revised form 6 July 2024; Accepted 8 July 2024
Available online 9 July 2024

interventions for MAFLD and strategies involve inhibiting hepatocyte pyroptosis to slow or reverse its progression, continues to be a focal point for researchers.

A significant number of experimental studies have conclusively shown the pivotal role of liver cell death in MAFLD [8–11], including apoptosis [12], necroptosis [13], pyroptosis [14] and ferroptosis [15]. A recently identified type of programmed death known as pyroptosis is characterized by extreme inflammation, content leaking, and swelling of the cells. Pyroptosis differs from other types of programmed death in its morphological features. Proinflammatory intracellular substances are released when the plasma membrane quickly bursts. Nuclear DNA lysis is also a part of PANoptosis, a distinct, physiologically relevant, inflammatory programmed cell death pathway that includes pyroptosis, apoptosis, and necroptosis. It is triggered by particular stimuli and controlled by the PANoptosome complex. Pyroptosis and apoptosis both involve nuclear DNA lysis [16]. A recent study has underscored the pivotal significance of pyroptosis in the progression of steatohepatitis [17], indicating its association with lipid deposition and exacerbation of liver fibrosis and inflammation. Gasdermin-D, along with its N-terminal fragment known as GSDMD-N, plays a crucial and fundamental role in the process of pyroptotic cell death. And both NASH patients and mouse models have elevated levels of this protein [18]. Furthermore, hepatic macrophages, commonly referred to as Kupffer cells, exhibit a distinctively high expression of the inflammasome NOD-, LRR- and pyrin domain-containing protein 3 (NLRP3), which significantly contributes to the induction of pyroptosis. Whereas hepatic stellate cells (HSCs) demonstrate a moderate level of expression of the same protein [19]. Interestingly, hepatocyte caspase-1-dependent NLRP3 overexpression was observed in knock-in mice with either global or myeloid-specific overexpression [20]. Apart from NLRP3, MAFLD exhibits a noteworthy affiliation with NOD-LRR- and pyrin domain-harboring 4 (NLRP4), two other integral components of the NLR family.According to certain studies, hepatocyte pyroptosis is induced by diacylglycerol (DAG) generated by sphingomyelin synthase 1 (SMS1) activated protein kinase Cδ(PKCδ) and NLR family CARD domain-containing protein 4 (NLRC4) inflammasome [21]. Activation and lysing of caspase 1 results in the production of IL-18 and IL-1β, which ultimately cause pyroptosis and release of proinfammatory cytokines. Some study [24] has also been conducted on the IL-18 and IL-1β that MAFLD releases during pyroptosis [22].

In oncology, pyroptosis has been shown to impede tumor development and metastasis by altering cell membrane permeability, stimulating the lysis and demise of tumor cell. GSDMD enhances the cytotoxic activity of T cells Recent research [23] has explored the relationship between pyroptosis and immune infiltration across various malignancies, However, the immune infiltration based on pytoptosis genes in MAFLD has not been thoroughly investigated.

The application of bioinformatics as a novel approach to explore disease pathways has gained significant traction. This technique is instrumental in identifying key genes associated with MAFLD, thereby advancing research into the pathophysiological processes underlying the disease [24]. In the present study, we have harnessed the prowess of bioinformatic techniques to delve into the intricacies of pyroptosis-associated genes in MAFLD. We posited that an all-inclusive exploration of these genetic underpinnings might afford us with profound insights into the immunologic landscapes of the disease, potentially revealing prospective therapeutic avenues for advancing drug development efforts in the foreseeable future.

2. Materials and methods

2.1. Data retrieval

From the GEO database, the expression profile datasets, GSE48452 [25], GSE63067 [26] and GSE89632 [27] for patients with MAFLD were downloaded utilizing the R package, GEOquery, for data retrieval and analysis [28]. All datasets were derived from *Homo sapiens*. To address batch effects, we employed the R package sva for de-batch processing, resulting in a combined dataset [29]. The inclusion criteria stipulated that patients must be at the minimum age of eighteen years, and furthermore, they should possess a liver biopsy-confirmed diagnosis of MAFLD, encompassing both uncomplicated hepatic steatosis as well as steatohepatitis. The exclusion criteria included malignancy and combining with other emergencies.

The GSE48452 dataset leveraged the Affymetrix human Gene 1.1 ST Array [transcript (gene) version], specifically the GPL11532 [HuGene-1_1-st] variant, as its data platform. For the GSE63067 dataset, the Affymetrix Human Genome U133 Plus 2.0 Array, designated as GPL570 [HG-U133_Plus_2], was selected as the preferred data platform. Meanwhile, the GSE89632 dataset relied on the Illumina HumanHT-12 WG-DASL V4.0 R2 expression beadchip platform, identified as GPL14951, for its data acquisition. The annotation of probe names for these datasets was accomplished with precision using the appropriate ChIP GPL platform files.

Drawing upon a variety of database sources, we successfully curated a collection of genes that are intricately linked to the process of pyroptosis. To ensure a comprehensive understanding of these human genes, we leveraged the GeneCards database [30] (https://www.genecards.org/) and additional genes were gathered from the GSEA database [31]. To find genes associated with pyroptosis, we used the term "pyroptosis" as the search term. Additionally, the cellular pyroptosis-related gene sets of [34,35] in the published literature were found using the search term "Pyroptosis-related Genes" on the PubMed website [32,33]. As outlined in Table S1, the final sample was procured following a rigorous process of deduplication.

2.2. DEGs associated with MAFLD

We utilized the R software DESeq2 [34] to acquire DEGs between distinct groups within the integrated dataset, with the objective of discovering the specific DEGs associated with MAFLD. The genes identified for further investigation were deemed as DEGs based on the criteria of having a |logFC| value greater than 0 and an adjusted p-value (adj.p) less than 0.05. The DEGs exhibiting upregulated expression, commonly referred to as upregulated genes, possessed a logFC value greater than 0 and an adjusted p-value less than 0.05.

Conversely, those DEGs demonstrating downregulated expression, or downregulated genes, exhibited a logFC value less than 0 and an adjusted p-value less than 0.05.

We created a Venn diagram by crossing the MAFLD dataset's DEGs with |logFC| value exceeding 0, an adjusted p-value (adj.p) less than 0.05 and the pyroptosis-related genes to generate PRDEGs associated with MAFLD. With the help of the R packages ggplot2, pheatmap, and RCircos, the differential expression analysis results were displayed as a heatmap, a volcano plot, and chromosome mapping [35].

2.3. Curve of the receiver operating characteristic

The Receiver Operating Characteristic (ROC) curve serves as an analytical tool for coordinate systems, enabling the selection of the most effective model, the elimination of suboptimal models, or the establishment of optimal thresholds within a given model [36]. As a comprehensive metric for continuous variables, the ROC curve showcases both sensitivity and specificity, highlighting the interplay between these two factors during the evaluation process. Conventionally, the Area Under the Curve (AUC) of an ROC curve spans from 0.5 to 1. Leveraging the survival ROC tool in R, we presented the PRDEG ROC curve for the MAFLD dataset and subsequently calculated the AUC to assess the diagnostic significance of PRDEG expression on the survival outcomes of MAFLD patients. A higher AUC value approaching 1 indicates a superior diagnostic performance, while AUC values ranging from 0.5 to 0.7 suggest poor accuracy, 0.7 to 0.9 moderate accuracy, and above 0.9 high accuracy.

2.4. Constructing a PRDEG-related diagnostic model

In order to create a diagnostic framework for pyroptosis-associated differentially expressed genes (PRDEGs) within the MAFLD dataset, we leveraged the robust glmnet package in R [37], specifically employing the LASSO (least absolute shrinkage and selection operator) regression technique. We fine-tuned the parameters to include a seed value of 2, set the family as "binomial," and iterated the regression process 1000 times, a precautionary measure to mitigate overfitting issues. The LASSO regression methodology, which is renowned for its prognostic modeling capabilities, not only minimizes the risk of overfitting but also elevates the model's versatility by incorporating a penalization factor. Additionally, we utilized forest plots to portray the expression patterns of each gene within the PRDEG diagnostic model. These LASSO-identified PRDEGs, henceforth referred to as LASSO genes, were subsequently subjected to a rigorous multivariate Cox regression analysis, ultimately resulting in the development of sophisticated multivariate Cox regression models.

Subsequently, we harnessed the R tool rms to fashion a refined nomogram, drawing from the outcomes of multivariate Cox regression analysis. The Nomogram [38]which serves as a visual interpretation of multivariate regression analysis, allows us to predict the likelihood of specific occurrences by aggregating cumulative scores and establishing a precise scoring scale for variables within the multivariate regression model. Following this, we evaluated the nomogram's accuracy and resolution through calibration analysis and the calibration curve.

Decision curve analysis (DCA) is a rapid technique for evaluating clinical prediction models, diagnostic tests, and molecular markers [39]. Finally, using the ggDCA R package to create DCA graphs, we assessed the precision and resolution of the Cox regression model [40].

2.5. Constructing a PRDEG-related LASSO genes risk model

Utilizing the median risk score as a pivotal criterion, individuals afflicted with MAFLD were divided into distinct categories of high and low risk through the implementation of LASSO regression analysis. It is determined how to calculate the risk score:

$$\text{riskScore} = \sum_{i} \text{Coefficient}\ (\text{gene}_i) * \text{mRNA Expression}\ (\text{gene}_i)$$

Pursuant to the analysis of risk scores, the prognostic significance of the LASSO genes in MAFLD patients was evaluated in both high and low risk categories. Ultimately, the R package survival ROC was employed, the patient survival time and survival status of ROC curves for LASSO genes in high and low risk groups were shown.

2.6. ssGSEA immune infiltration analysis

The single-sample gene-set enrichment analysis (ssGSEA) technique was used to determine the relative abundance of each immune cell infiltrate [41]. Activated $CD8^+$ T cells, activated dendritic cells, gamma delta T cell, natural killer T cells, and regulatory T cells were just a few of the immune cell subtypes that were identified as invading. The relative abundance of each immune cell infiltration was represented by enrichment scores computed by ssGSEA for each sample. The MAFLD dataset's diverse illness subtypes were subsequently analyzed utilizing the ggplot2 tool for the purpose of visually depicting the correlation between the differential expression of immune cells. The utilization of the R package pheatmap depicted analysis to pertinence of the hub genes in various MAFLD risk groups, as well as the outcomes of LASSO gene expression in various disease subtypes.

2.7. Protein-protein interaction network

Individual proteins involved in biological signaling, protein-protein interaction (PPI) networks are composed of mechanisms that control gene expression, drug and energy metabolism, and cell cycle regulation. The STRING database [42] offers a platform for exploring the known proteins, and it can predict intricate interactions occurring among these biomolecules. A PPI network was constructed in this study using LASSO regression and the STRING database (minimum required interaction score: medium confidence [0.400]), and the PPI network model was then displayed using Cytoscape(version 3.9.1 was downloaded from https://cytoscape.org/) [43], which are: Maximum Neighborhood Component (MNC), the Degree, Maximal Clique Centrality (MCC) [44]were employed to obtain the pivotal hub genes. In the PPI Network, the scores of LASSO genes are calculated and then arranged according to the scores. Finally, the genes identified by these three distinct algorithms were intersected and subjected to an in-depth analysis using a Venn diagram. The hub gene associated with pyroptosis was one of the algorithm's intersection genes.

2.8. Establishment of the transcription factor-mRNA and mRNA-miRNA interaction networks

Through their interactions with target genes (mRNA), transcription factors (TF) regulate gene expression at the post-transcriptional stage. The regulatory impact of transcription factors on the hub genes linked to pyroptosis was examined using the transcription factors found in the ChIPBase database [45], and Cytoscape software was used to show the TF-mRNA regulatory network.

Numerous target genes can be regulated by a single miRNA, and different miRNAs may control the same target gene. MiRNAs play a significant regulatory function in the evolution of biological development. The miRNA linked to the hub gene was found using the StarBase database [48] in order to study the interaction between hub genes relevant to pyroptosis and miRNAs. The network of mRNA-miRNA regulation was shown using software.

2.9. Differential gene functional enrichment analysis and pathway enrichment analysis

The Gene Ontology (GO) [46]analysis method is frequently employed in extensive functional enrichment investigations, encompassing biological processes (BP), molecular functions (MF), and cellular components (CC). The Kyoto Encyclopedia of Genes and Genomes (KEGG) a renowned database, serves as a repository for information pertaining to genomes, biological processes, diseases, and medications [47]. The hub genes associated with pyroptosis were analyzed for GO annotation using the clusterProfiler [48] of the R package. The selection threshold for screening entries was set at $P < 0.05$ and a False Discovery Rate (FDR) value, also known as the q-value, of less than 0.05. Both these metrics were considered statistically significant. Following that, the Benjamini-Hochberg (BH) approach was implemented to adjust the P-value.

2.10. Gene set enrichment analysis

To precisely determine the individual contribution of each gene towards shaping the phenotype, we employ the gene set enrichment analysis (GSEA) approach to analyze the distribution trend of each gene inside a pre-defined gene set in a list of genes rated by phenotypic correlation. In the present study, the genes within the MAFLD dataset have been segregated into two distinct groups, based on their correlation to specific phenotypic characteristics.Then, we enriched all DEGs in phenotypic correlation using the clusterProfiler tool. The following were the criteria utilized in the GSEA: 2020, 1000 calculations, 10 gene sets, and a maximum of 500 genes. The BH technique was employed to refine and adjust the P-values, ensuring greater precision. The c2.cp.v7.2.symbols gene set was sourcedfrom the Molecular Signatures Database (MSigDB) [49]. The selection criteria for highly enriched genes were $P < 0.05$ and FDR value (q.value) < 0.25.

2.11. CIBERSORTx immune infiltration analysis

CIBERSORTx is a tool based on linear support vector regression to estimate immune cell composition and abundance in mixed cells by deconvolving transcriptomic expression matrices [50]. We uploaded the gene expression matrix data to CIBERSORTx, and combined the LM 22 eigengene matrix to screen samples with p value < 0.05 to obtain the immune cell infiltration matrix. The samples with zero immune cell enrichment scores were subsequently filtered out to obtain accurate immune cell infiltration data. Ultimately, a comprehensive visualization of the results was achieved through the creation of a correlation heat map using the R program pheatmap, and the distribution of the 22 immune cell infiltrates across samples was graphically depicted using the R program ggplot2.

2.12. Construction of disease subtypes based on pyroptosis-related hub genes

Consensus Clustering [51] serves as a resampling-centric algorithm that identifies and validates the rationality of each member and its subgroup number. Furthermore, it rigorously verifies the validity and robustness of the clustering outcome, ensuring a comprehensive and dependable assessment of the data groupings. To gain a deeper understanding of the heterogeneity of the disease by categorizing the diverse subtypes of MAFLD disease, we employed the robust consensus clustering method provided by the comprehensive ConsensusClusterPlus package in R [52], focusing on pyroptosis-associated hub genes.

2.13. Cell culture and treatment

In the realm of in vitro scientific endeavors, Procell Life Science & Technology, located in Wuhan, Hubei province, China, provided mouse hepatocytes of the AML12 cell line. These AML12 cells were cultured in Dulbecco's Modified Eagle Medium (DMEM), maintained at a temperature of 37 °C in a humidified atmosphere containing 5 % CO_2, and further supplemented with 10 % (v/v) fetal bovine serum and 1 % penicillin/streptomycin for optimal growth conditions. Subsequently, the AML12 cells were exposed to a treatment comprising 1 mM of free fatty acids (FFA), specifically a blend of oleic acid (OA) and palmitic acid (PA) in a 2:1 volumetric ratio, within a complete medium for 24 h [53].This approach culminated in the successful development of a fatty liver cell (FLC) model. The steatohepatitis cell model (SHC) was successfully established through the administration of methionine-choline and glutamine deficient (MCD) medium to the cells for a duration of 24 h [18].

2.14. Reverse transcription quantitative polymerase chain reaction (RT-qPCR)

To ensure precise and efficient extraction of total RNA, the trizol reagent was employed. Moreover, TOYOBO (Japan) kindly supplied the RT kit, which facilitated the reverse transcription process. Subsequently, we conducted RT-qPCR utilizing the SYBR Green qRT-PCR Mix, sourced from Solarbio, Beijing, China. This assay allowed us to accurately quantify the relative expression levels, utilizing the $2-\Delta\Delta CT$ method with GAPDH serving as the internal reference gene for normalization. The specific forward and reverse primers that we employed are detailed below.:

HSP90AA1 (F: '-ACGAATTCAATGCCCGAGGAAACCCA', R: 5′-GCTCTAGACTAATCGACTTCCTCCATGCG-3′);
CDK9 (F: 5′-ACTTCTGCGAGCATGACCTT', R: 5′-AAAGTCTGCCAGCTTCAGGA-3′);
TSLP (F: 5′-CGTAAACTTTGCCGCCTATGA', R: 5′-TTCTTCATTGCCTGAGTAGCATTTAT-3′);
BRD4 (F: 5′-TGAGTCGGAGGAAGAGGACAAGTG', R: 5′-CGCAGTGTGGACGGCTTCAG3′);
GAPDH (F: 5′-GCATCCACTGGTGCTGCC-3′, R: 5′-TCATCATACTTGGCAGGTTTC-3′).

2.15. Statistical analysis

All data processing and analysis in this work was conducted using the R software (Version 4.2.0). Continuous variables are represented by the average, denoted as the mean ± standard deviation, whereas the data that are not distributed normally are succinctly summarized by their median value. For comparisons between two groups, the Wilcoxon rank sum test was employed, and for comparisons among three or more groups, the Kruskal-Wallis test was utilized. To evaluate the statistical significance of categorical variables between two groups, we employed either Fisher's exact test or the chi-square test. Unless specified otherwise, the analysis of

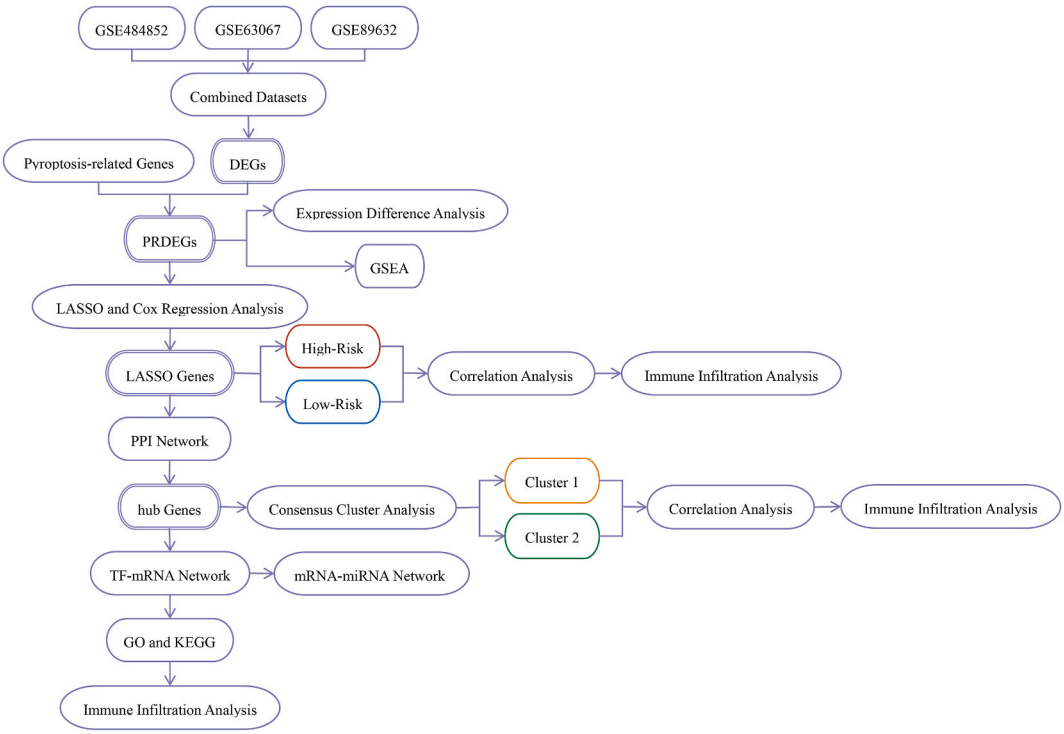

Fig. 1. Technical roadmap.

all data was conducted using Spearman correlation analysis to determine the correlation coefficients between various compounds. A significant difference was defined as having a P-value less than 0.05.

Additionally, GraphPad Prism software (GraphPad Prism Software, CA, United States) was harnessed to delve into the PCR data, offering a comprehensive analysis. For comparisons involving two groups, the Student's unpaired *t*-test was executed, while for multi-group comparisons, the one-way ANOVA test was employed. The results were deemed statistically significant if the p-value fell below the critical threshold of 0.05.

3. Results

3.1. Roadmap of pyroptosis-related genes analysis in MAFLD

We designed the technical roadmap (Fig. 1) to do a comprehensive analysis of pyroptosis-related genes in MAFLD.

3.1.1. Extracted data

A cumulative number of 91 cases were obtained from the GEO database, comprising 46 MAFLD samples and 45 normal samples. Dataset GSE 48452 contains 73 samples: 18 MAFLD samples, 14 control samples, 27 healthy obesity samples and 14 steatosis samples; only MAFLD samples (group: MAFLD) and control samples (group: Normal) were included in this study. Dataset GSE63067 contains 18 samples: 9 MAFLD samples, 7 control samples and 2 steatosis samples; only MAFLD samples, (group: MAFLD) and control (group: Normal) samples were included in this study. Dataset GSE89632 contains 63 samples: 19 MAFLD samples, 24 control samples and 20 steatosis samples; only MAFLD samples (group: MAFLD) and control (group: Normal) samples were included in this study, Obesity and steatosis group samples were not included in the study. The detailed information pertaining to the specific dataset is concisely outlined in Table 1. A total of 322 cell pyroptosis-related genes were obtained, as described in Table S1.

3.2. Identification of differentially expressed genes (DEGs) in MAFLD

After removing the batch effects on the three MAFLD dataset, we obtained combined datasets. The results of distribution boxplot and the principal component analysis(PCA) performed on the dataset's expression matrix, we were able to affirm the successful elimination of batch effects in the MAFLD dataset, both before and after the removal process (Fig. 2A–D).The combined GEO dataset was divided into two groups encompassed 46 MAFLD-specific samples (categorized as MAFLD group) alongside 45 control samples (categorized as Normal group). In order to delve into the differences in gene expression between the MAFLD group and the Normal group, we employed the R package DESeq2 to gather and analyze the differentially expressed genes (DEGs) across the various groups within the MAFLD dataset. The findings were outlined as follows: precisely 2177 differentially expressed genes (DEGs) in the MAFLD dataset met the stringent criteria of |logFC| exceeding 0 and an adjusted p-value beneath 0.05. At this threshold, we observed a notable imbalance, with 1170 genes exhibiting an upregulation (positive logFC), while 1007 genes displayed a downregulation (negative logFC). To visually illustrate these findings, we crafted a Volcano plot, as depicted in Fig. 3A. To obtain the PRDEGs, we identified all differentially expressed genes (DEGs) that exhibited a |logFC| greater than 0 and an adjusted p-value less than 0.05. Subsequently, we determined the intersection of these genes with those related to pyroptosis. After comprehensive analysis, a comprehensive list (Table 2) encompassing a total of 44 PRDEGs for MAFLD diseases was successfully compiled. Furthermore, a Venn diagram was skillfully crafted to illustrate the intricate relationships among these genes (Fig. 3B). We conducted a thorough analysis of the differential expression patterns of 44 PRDEGs. Leveraging the results garnered from the Venn diagram we utilized the R package pheatmap to generate a heat map that vividly depicts the specific findings of our differential analysis (Fig. 3C). Finally, the location of 44 PRDEG on the human chromosome were analyzed by R package RCircos (Fig. 3D). Chromosome localization maps showed that, Gene EPHA 2, GBP5, IFI 16 and ATF 6 were precisely situated on chromosome 1; DNMT3A, LRPPRC, IL 1 A and IFIH 1 were located on chromosome 2; CASP6, TLR 2 and TLR 3 were found on chromosome 4; NAIP and TSLP were positioned on chromosome 5; TNF and GJA 1 were located on chromosome 6; IL 6 was located on chromosome 7; LY96, GSDMC and VPS 28 were situated on chromosome 8; CDK9, NINJ 1 and CD274 were found on chromosome 9; GSTO 1 and PRF 1 were positioned on chromosome 10; DRD2, CASP4, BIRC2, PANX1, FADD and TRAF 6 were located on chromosome 11; MDM 2 was located on chromosome 12; HSP90AA1 and CTSG were mapped on chromosome 14; NEDD 4 was situated on chromosome 15; E2F4 was located on chromosome 16; SUZ 12 was located on chromosome 17; MALT 1 was located on chromosome 18; BAX, BRD 4 and DPP9 were found on chromosome 19; ZBP 1 and DNMT3B

Table 1
GEO microarray chip information.

	GSE48452	GSE63067	GSE89632
Platform	GPL11532	GPL570	GPL14951
Species	*Homo sapiens*	*Homo sapiens*	*Homo sapiens*
Tissue	Liver	Liver	Liver
Samples in MAFLD group	18	9	19
Samples in Normal group	14	7	24
Reference	PMID: 23931760	PMID: 25993042	PMID: 25581263

GEO,Gene Expression Omnibus.

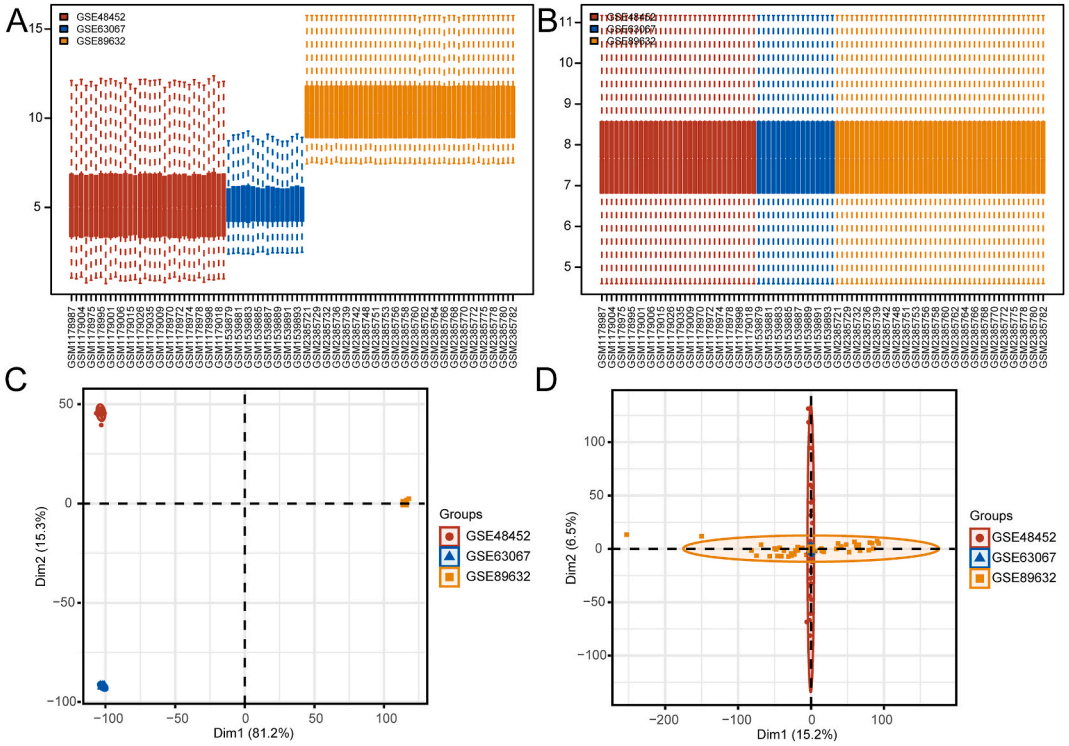

Fig. 2. The De-batch processing of the MAFLD dataset.
(A–B) The MAFLD dataset undergoes a rigorous batch effect removal process. Specifically, (A) illustrates the boxplot representation prior to processing, whereas (B) displays the refined boxplot after the de-batching treatment. (C–D)The MAFLD dataset exhibits a distinct reduction in batch effect through PCA. (C) The before de-batch processing PCA plot (D) the PCA plot after the de-batching procedure. In these plots, dataset GSE48452 is represented in red, dataset GSE63067 in blue, and dataset GSE89632 in orange. MAFLD:metabolic dysfunction-associated fatty liver disease.

were located on chromosome 20; The RBBP 7 was located on the X chromosome.

3.3. Analysis of pyroptosis-related differentially expressed genes (PRDEGs)

To further explore the expression differences of PRDEGs in the MAFLD dataset, the expression differences of the 44 PRDEGs between the MAFLD and Normal groups were demonstrated by group comparison the boxplots (Fig. 4A). As is distinctly illustrated in Fig. 4A, the expression of all 44 PRDEGs was statistically significant between the different groups in the MAFLD dataset ($P < 0.05$). Among these, the expression levels of the genes IFIH 1, BRD4, TNF, MALT1, LY96, DPP9, SUZ12, IFI16, NINJ1, TLR3, PRF1, DNMT3B, IL1A, RBBP7, GSDMC, LRPPRC, E2F4, CD274, CASP6, NAIP, VPS28, EPHA2, PANX1, TSLP, DRD2, ATF6, TRAF6 and IL6 were extremely statistically significant between the different groups in the MAFLD dataset ($P < 0.001$). Additionally, the expression levels of genes GSTO1, DNMT3A, FADD, GJA1, MDM2, BAX, HSP90AA1, ZBP1, CASP4, CDK9, CTSG, BIRC2, FPR2, GBP5, NEDD4 and TLR2 were also highly statistically significant between the different groups in the MAFLD dataset with ($P < 0.01$).

Subsequently, we drew the ROC curves of 44 PRDEGs in the MAFLD dataset and presented the results (Fig. 4B–J). The ROC curve results were as follows: the expression levels of 29 PRDEGs showed a moderate correlation($0.7 < AUC < 0.9$) between the MAFLD samples (group: MAFLD) and control sample (grouping: Control) in the MAFLD dataset. The 29 PRDEGs were IFIH1, BRD4, TNF, MALT1, LY96, DPP9, SUZ12, IFI16, NINJ1, TLR3, PRF1, DNMT3B, IL1A, RBBP7, GSDMC, LRPPRC, E2F4, CD274, CASP6, NAIP, VPS28, EPHA2, PANX1, TSLP, DRD2, ATF6, TRAF6, IL 6 and NEDD4. The expression levels of 15 PRDEGs showed a moderate correlation($0.5 < AUC < 0.7$)between different groups. The 15 PRDEGs were: GSTO 1, DNMT3A, FADD, GJA1, MDM2, BAX, HSP90AA1, ZBP1, CASP4, CDK9, CTSG, BIRC2, FPR2, GBP5 and TLR2.

3.4. Differential expression and prognostic value of PRDEGs in MAFLD

We employed the LASSO regression analysis methodology to create a PRDEG diagnostic model, gauging the diagnostic efficacy and accuracy of the 44 selected PRDEGs within the MAFLD dataset (Fig. 5A). The LASSO variable trajectory map, where the y-axis indicates net income, was also obtained and used to display the LASSO regression results. (Fig. 5B). The analysis revealed that 20 pyroptosis-related LASSO genes were used to construct the LASSO diagnostic model. These genes are BRD4, MALT1, DPP9, SUZ12, TLR3, PRF1, DNMT3B, IL1 A, E2F4, VPS 28, PANX1, TSLP, DRD2, DNMT3A, ATF6, HSP90AA1, CASP4, CDK9, GBP5, and NEDD4. The expression

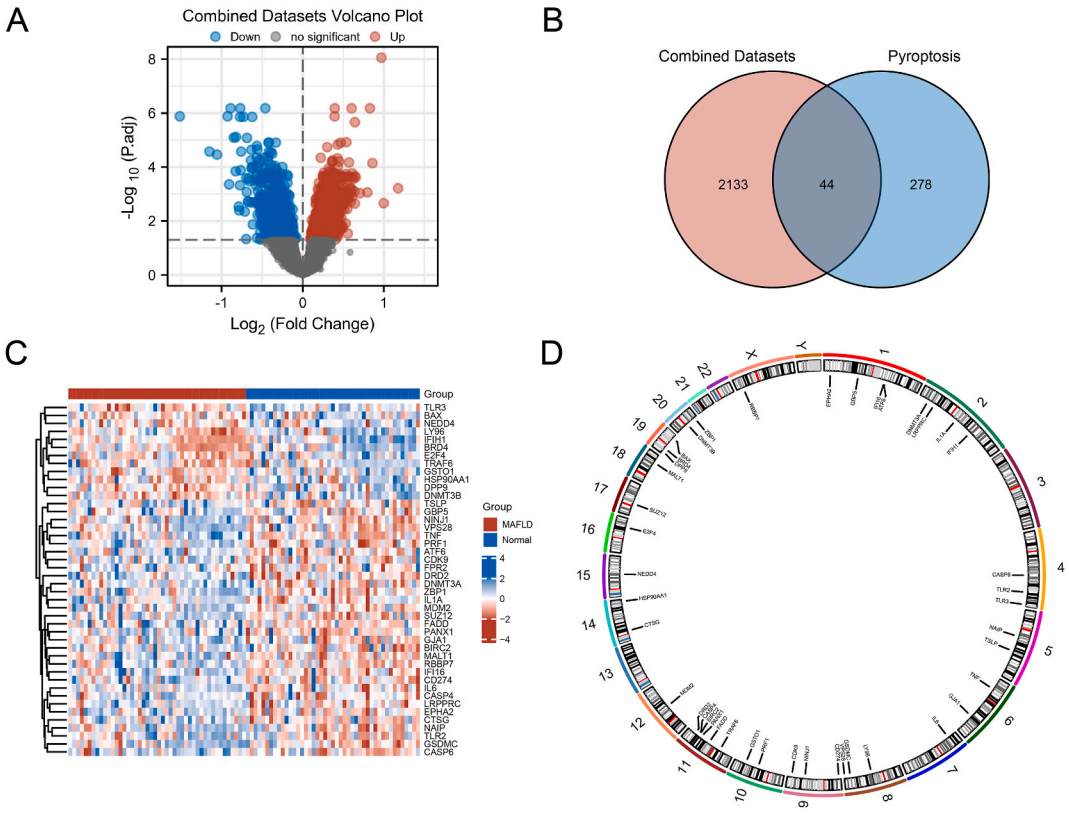

Fig. 3. Differential gene expression analysis conducted on the MAFLD dataset.
(A) The volcano plot of differential gene analysis between MAFLD and Normal groups in the Combined Datasets.(B) The wayn diagram of differentially expressed genes (DEGs) and pyroptosis-related genes in the integrated GEO dataset (C) The comprehensive numerical heatmap representation of the PRDEGs within the MAFLD dataset. (D) The chromosome localization map depicts the precise positions of PRDEGs.

levels of 20 LASSO genes across distinct groups were visualized employing a forest map (Fig. 5C).

Subsequently, we conducted univariate and multivariate Cox regression analyses using the 20 PRDEGs and constructed a Cox regression model The prognostic capability of the model and the nomogram was displayed through nomogram analysis (Fig. 5D). Additionally, a Calibration analysis was executed utilizing the calibration graph (Calibration Curve), in order to assess the precision of the model by evaluating the congruency between the actual probability and the predicted probability (Fig. 5E). Finally, we assessed the developed Cox regression model's clinical value using DCA, and Fig. 5F shows the findings.

3.5. *Comprehensive analysis of the diagnostic and prognostic capabilities of the PRDEG model*

To examine how the pyroptosis-related risk model affects patients' development of MAFLD. Utilizing the median expression value derived from the LASSO regression analysis, patients suffering from MAFLD were categorically divided into two distinct groups: those at a higher risk and those at a lower risk. To deeply analyze the disparities in LASSO gene expression among the two distinct groups, we crafted an intricate boxplot (depicted in Fig. 6A) that vividly portrays the varying expression levels of 20 pyroptosis-associated LASSO genes (hereinafter referred to as 'LASSO Genes'). The comprehensive analysis of this chart revealed that the differential expression of a noteworthy 10 pyroptosis-linked LASSO genes was statistically significant, evidenced by a p value that fell below the critical threshold of 0.05. Among the examined genes, the expression levels of VPS 28 exhibited a highly significant statistical difference between the two groups in the MAFLD dataset ($P < 0.001$). Similarly, the expression levels of BRD4, DNMT3B, and E2F4 also displayed significant statistical differences ($P < 0.01$). Furthermore, the statistical analysis revealed significant results of the expression levels of MALT1, DPP9, SUZ12, TLR3, PRF1, and DNMT3A ($P < 0.05$) when comparing the two groups. Furthermore, the comparative expression levels of numerous genes, including IL1A, PANX1, TSLP, DRD2, AT6, HSP90AA1, CASP4, CDK9, GBP5, and NEDD4, did not yield any statistically significant differences between the two groups ($P \geq 0.05$).

Subsequently, we analyzed the receiver operating characteristic (ROC) curves of 10 LASSO genes, as depicted in Fig. 6B–K. The findings indicate a robust correlation in the expression levels of 5 genes between the high-risk and low-risk groups, with an area under the curve (AUC) ranging from 0.7 to 0.9.The 5 pyroptosis-related LASSO genes were: BRD4 (Fig. 6B, AUC = 0.764), PRF1(Fig. 6G, AUC = 0.713), DNMT3B (Fig. 6H, AUC = 0.732), E2F4(Fig. 6I, AUC = 0.766) and VPS 28 (Fig. 6J, AUC = 0.802). The expression levels of other 5 LASSO genes showed a low correlation($0.5 < AUC < 0.7$). The 5 pyroptosis-related LASSO genes were: MALT 1 (Fig. 6C, AUC =

Table 2
Results of pyroptosis-related differentially expressed genes.

Gene Symbol	Description	logFC	AveExpr	p value	adj.p value
IFIH1	Interferon Induced With Helicase C Domain 1	−1.15E+00	7.88E+00	5.44E-08	2.68E-05
BRD4	Bromodomain Containing 4	−3.92E-01	6.94E+00	5.99E-08	2.81E-05
TNF	Tumor Necrosis Factor	4.71E-01	7.66E+00	2.01E-06	2.52E-04
MALT1	MALT1 Paracaspase	3.07E-01	8.27E+00	2.31E-06	2.69E-04
LY96	Lymphocyte Antigen 96	−5.78E-01	1.01E+01	2.88E-06	3.15E-04
DPP9	Dipeptidyl Peptidase 9	−3.66E-01	1.02E+01	1.45E-05	9.35E-04
SUZ12	SUZ12 Polycomb Repressive Complex 2 Subunit	2.88E-01	8.02E+00	2.04E-05	1.17E-03
IFI16	Interferon Gamma Inducible Protein 16	5.28E-01	7.83E+00	2.27E-05	1.26E-03
NINJ1	Ninjurin 1	3.99E-01	9.81E+00	4.43E-05	1.89E-03
TLR3	Toll Like Receptor 3	−3.46E-01	8.84E+00	8.66E-05	2.87E-03
PRF1	Perforin 1	4.17E-01	8.37E+00	9.04E-05	2.94E-03
DNMT3B	DNA Methyltransferase 3 Beta	−1.96E-01	7.05E+00	1.03E-04	3.18E-03
IL1A	Interleukin 1 Alpha	3.00E-01	9.17E+00	1.29E-04	3.73E-03
RBBP7	RB Binding Protein 7, Chromatin Remodeling Factor	1.90E-01	9.89E+00	1.39E-04	3.93E-03
GSDMC	Gasdermin C	2.92E-01	1.00E+01	1.66E-04	4.51E-03
LRPPRC	Leucine Rich Pentatricopeptide Repeat Containing	2.45E-01	1.04E+01	2.62E-04	5.97E-03
E2F4	E2F Transcription Factor 4	−3.72E-01	7.75E+00	2.63E-04	5.97E-03
CD274	CD274 Molecule	3.62E-01	8.61E+00	3.13E-04	6.75E-03
CASP6	Caspase 6	2.42E-01	7.79E+00	3.89E-04	7.73E-03
NAIP	NLR Family Apoptosis Inhibitory Protein	2.16E-01	8.31E+00	3.92E-04	7.75E-03
VPS28	VPS28 Subunit Of ESCRT-I	4.04E-01	7.45E+00	4.10E-04	7.96E-03
EPHA2	EPH Receptor A2	3.51E-01	8.64E+00	5.43E-04	9.41E-03
PANX1	Pannexin 1	1.67E-01	7.73E+00	7.18E-04	1.11E-02
TSLP	Thymic Stromal Lymphopoietin	3.26E-01	7.32E+00	8.42E-04	1.22E-02
DRD2	Dopamine Receptor D2	2.24E-01	9.96E+00	1.01E-03	1.36E-02
GSTO1	Glutathione S-Transferase Omega 1	−2.81E-01	8.32E+00	1.17E-03	1.49E-02
DNMT3A	DNA Methyltransferase 3 Alpha	1.68E-01	9.88E+00	1.32E-03	1.60E-02
FADD	Fas Associated Via Death Domain	1.86E-01	6.97E+00	1.47E-03	1.71E-02
ATF6	Activating Transcription Factor 6	4.95E-01	7.50E+00	1.66E-03	1.83E-02
GJA1	Gap Junction Protein Alpha 1	2.76E-01	6.54E+00	1.75E-03	1.89E-02
MDM2	MDM2 Proto-Oncogene	1.49E-01	7.78E+00	1.80E-03	1.93E-02
TRAF6	TNF Receptor Associated Factor 6	−4.48E-01	7.97E+00	1.97E-03	2.04E-02
IL6	Interleukin 6	3.37E-01	8.20E+00	2.24E-03	2.22E-02
BAX	BCL2 Associated X, Apoptosis Regulator	−1.46E-01	6.95E+00	2.43E-03	2.34E-02
HSP90AA1	Heat Shock Protein 90 Alpha Family Class A Member 1	−1.72E-01	7.63E+00	2.53E-03	2.40E-02
ZBP1	Z-DNA Binding Protein 1	1.28E-01	8.28E+00	3.11E-03	2.75E-02
CASP4	Caspase 4	2.92E-01	8.97E+00	3.19E-03	2.80E-02
CDK9	Cyclin Dependent Kinase 9	2.56E-01	7.77E+00	3.47E-03	2.96E-02
CTSG	Cathepsin G	2.25E-01	7.88E+00	3.61E-03	3.05E-02
BIRC2	Baculoviral IAP Repeat Containing 2	2.55E-01	8.51E+00	4.64E-03	3.63E-02
FPR2	Formyl Peptide Receptor 2	3.30E-01	7.98E+00	4.76E-03	3.69E-02
GBP5	Guanylate Binding Protein 5	2.47E-01	9.64E+00	5.41E-03	4.04E-02
NEDD4	NEDD4 E3 Ubiquitin Protein Ligase	−1.93E-01	7.16E+00	6.05E-03	4.33E-02
TLR2	Toll Like Receptor 2	2.92E-01	7.69E+00	6.78E-03	4.67E-02

0.692), DPP9(Fig. 6D, AUC = 0.675), SUZ12(Fig. 6E, AUC = 0.682), TLR3(Fig. 6F, AUC = 0.682) and DNMT3A (Fig. 6K, AUC = 0.691).

3.6. PRDEG-related risk model and immuno-infiltration analysis

To comprehensively analyze the disparity in immune infiltration among MAFLD patients in high-risk and low-risk groups, the ssGSEA algorithm was employed to gauge the proliferation of immune cells in both cohorts. Subsequently, group comparison boxplots were utilized to visually illustrate these findings, highlighting the statistical significance of 5 distinct immune cell types in Fig. 7A ($P < 0.05$). In the analysis, the variation in T follicular helper cell count between the high-risk and low-risk groups was highly significant, with a p-value of less than 0.001. Additionally, the Central memory CD8 T cell also demonstrated a notable significance, with a p-value less than 0.01. Furthermore, the statistical analysis revealed statistically significant differences in the expression levels of Activated CD4 T cell, CD56dim natural killer cell, and Neutrophil, with a p-value of less than 0.05.

Based on the results of the ssGSEA immune infiltration analysis, a correlation heatmap was generated to assess the statistical significance of immune cell infiltration abundance in the high-risk group (Fig. 7B) and low-risk group (Fig. 7C) within the MAFLD dataset. The results indicate that in the high-risk group, the highest correlation was observed between Central memory CD8 T cells and T follicular helper cells (correlation value = 0.37), whereas in the low-risk group, the strongest association was noted between Activated CD4 T cells and T follicular helper cells (correlation value = 0.67). Furthermore, the correlation heatmap was utilized to investigate the relationship between the frequency of five immune cell infiltrations and the expression of twenty LASSO genes in both risk groups (Fig. 7D–E). The analysis revealed that in the high-risk group, DPP9 and CD56dim natural killer cells exhibited a clear

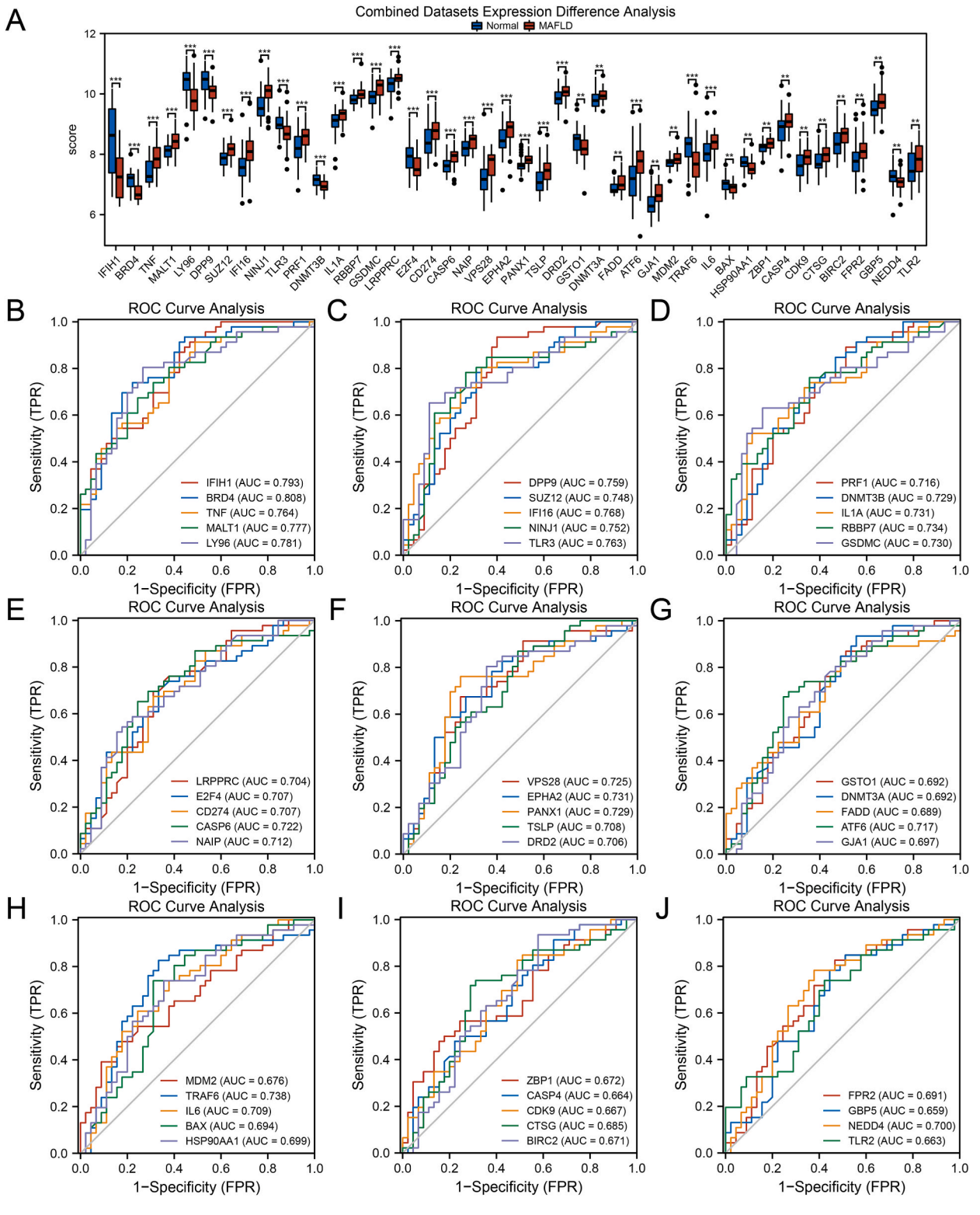

(caption on next page)

Fig. 4. PRDEGs expression difference and ROC curve analysis.
(A) The boxplot of differential expression analysis of PRDEGs in the MAFLD Datasets. (B-J) The ROC curves of 44 PRDEGs in MAFLD dataset. The symbol "ns" is analogous to a P-value greater than or equal to 0.05, indicating the absence of statistical significance; conversely, the symbol "*" represents a P-value less than 0.05, thus indicating statistical significance. Furthermore, the double asterisk "**" signifies a P-value less than 0.01, denoting a high level of statistical significance. Lastly, the triple asterisk "***" corresponds to a P-value less than 0.001, which is also indicative of a profound statistical significance.

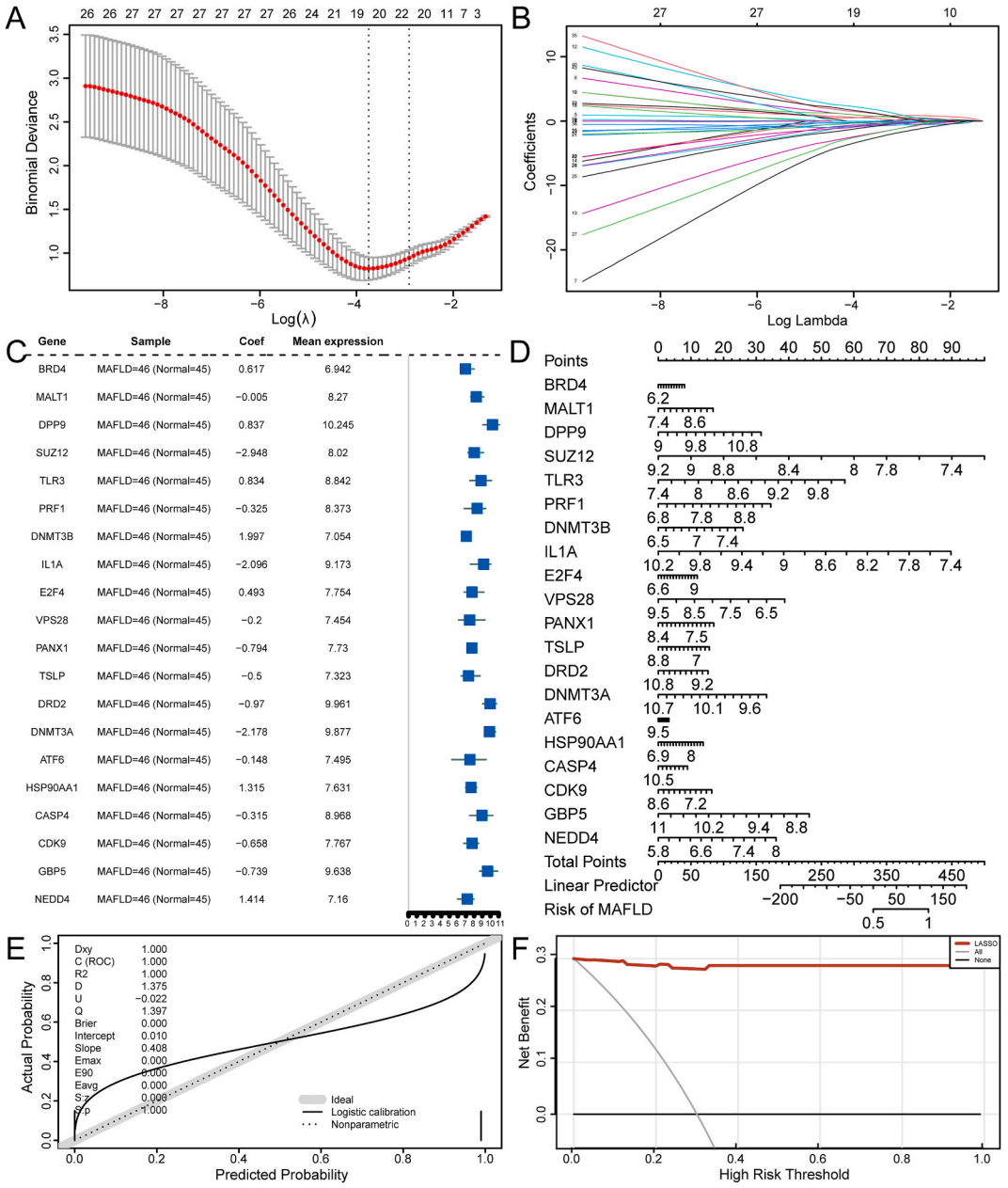

Fig. 5. The development of the PRDEG diagnostic model and its assessment in terms of prognostic performance.
(A) The LASSO regression model used for the PRDEG diagnostic model of MAFLD. The parameters are set to set.seed (2) and family = "binomial"and iterated the regression process 1000 times. (B) The variable trajectory plot of PRDEGs in the LASSO diagnostic model for MAFLD. (C) The forest plot portraying PRDEGs within the LASSO diagnostic model for MAFLD. (D)The Nomogram plot, (E) the calibration curve plot, (F) the DCA plot of the PRDEG univariate and multivariate Cox regression models in the PRDEG diagnostic model. The DCA figure has a y-axis for net income and an x-axis for probability threshold or threshold probability. By examining the x value range of the lines of All positive and All negative, the outcome may be determined. The model effect is enhanced by a wide x value range.

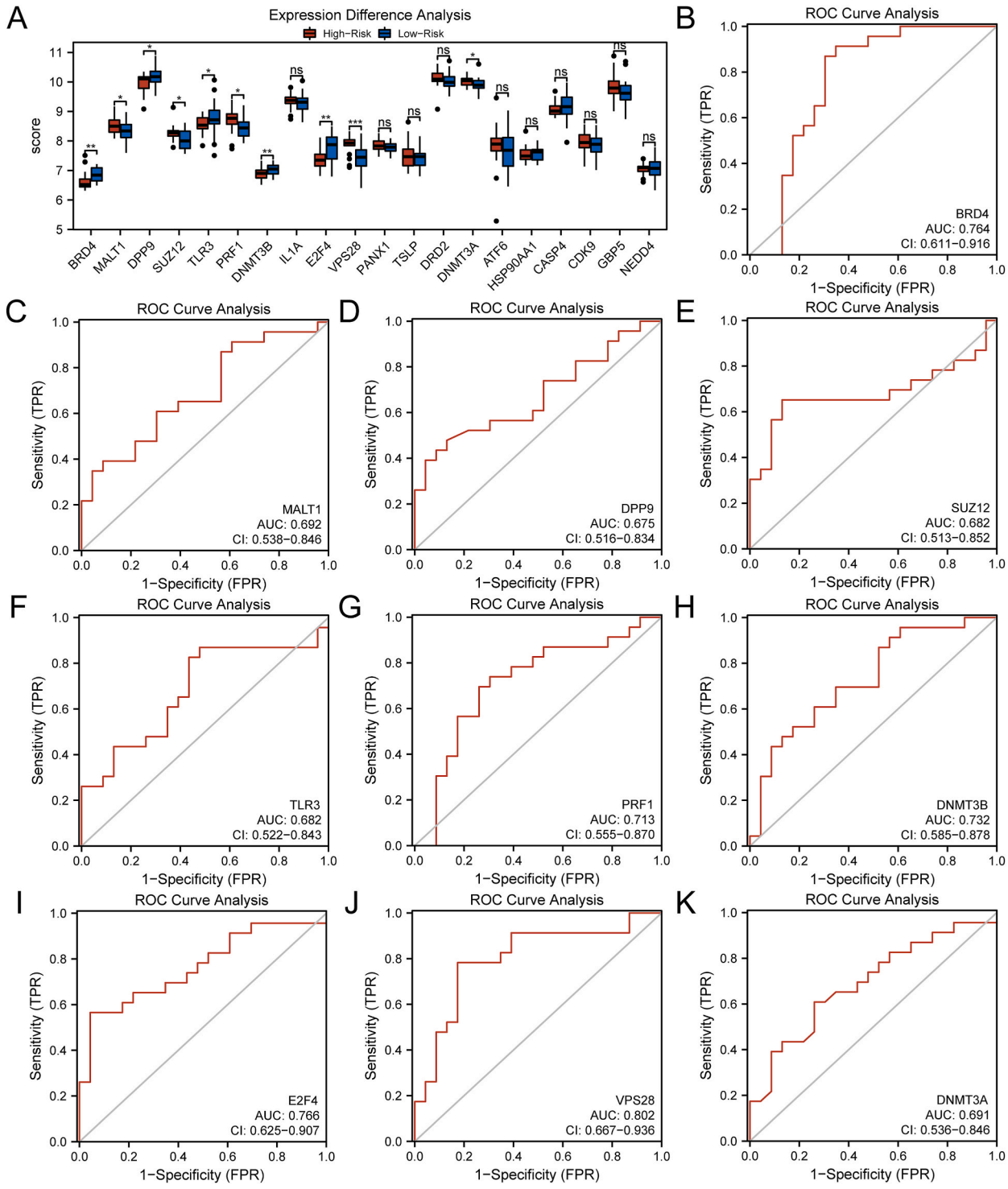

Fig. 6. Risk score analysis for LASSO genes.
(A) Group comparison plot of the PRDEG-related LASSO genes expression difference analysis in the high risk and low risk groups in the MAFLD dataset. (B–K) The ROC curves of LASSO genes BRD 4 (B), MALT 1 (C), DPP9 (D), SUZ 12 (E), TLR 3 (F), PRF 1 (G), DNMT3B (H), E2F4 (I), VPS 28 (J), and DNMT3A (K) in the high risk and low risk groups in MAFLD dataset. Blue is the low risk group and red is the high risk group. The symbol "ns" is analogous to a P-value greater than or equal to 0.05, indicating the absence of statistical significance; conversely, the symbol "*" represents a P-value less than 0.05, thus indicating statistical significance. Furthermore, the double asterisk "**" signifies a P-value less than 0.01, denoting a high level of statistical significance. AUC has a low accuracy at 0.5–0.7, and AUC has moderate accuracy at 0.7–0.9.

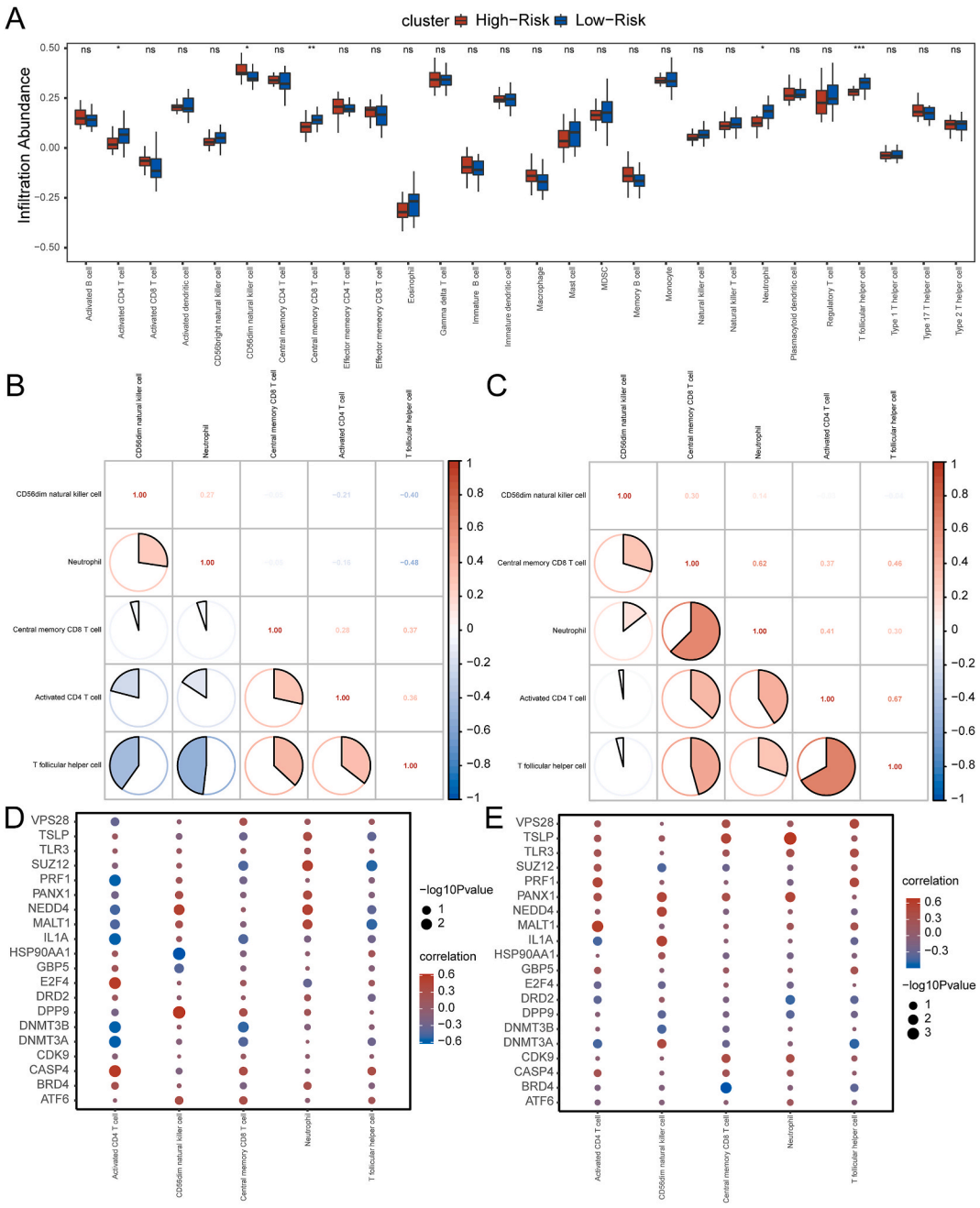

Fig. 7. Risk Group Immune Infiltration Analysis by ssGSEA Algorithm.
(A) Group comparison of results of ssGSEA immune infiltration analysis between the high risk and low risk groups. (B–C) Results of the correlation analysis of 5 immune cells infiltration abundance in the high risk group(B) and low risk group(C) are shown. (D–E) Heatmap of the correlation between immune cells and LASSO genes in the high risk group (D) the low risk group (E). The symbol "ns" is analogous to a P-value greater than or equal to 0.05, indicating the absence of statistical significance; conversely, the symbol "*" represents a P-value less than 0.05, thus indicating statistical significance. Furthermore, the double asterisk "**" signifies a P-value less than 0.01, denoting a high level of statistical significance. Lastly, the triple asterisk "***" corresponds to a P-value less than 0.001, which is also indicative of a profound statistical significance.

positive correlation, whereas HSP90AA1 and CD56dim natural killer cells showed a significant negative correlation. Conversely, in the low-risk group, TSLP and Neutrophil were positively correlated, while BRD4 and Central memory CD8 T cells exhibited a distinct negative correlation.

3.7. PPI interaction networks and screening of hub genes

Utilizing the STRING database, we established the PPI Network for the 20 pyroptosis-linked LASSO genes. The intricate interaction patterns were subsequently rendered visible through the utilization of Cytoscape software (Fig. 8A). Among these, a noteworthy 15 pyroptosis-linked LASSO genes BRD4, SUZ12, TLR3, PRF1, DNMT3B, IL1A, E2F4, VPS28, TSLP, DNMT3A, ATF6, HSP90AA1, CASP4, CDK9, and NEDD4, each playing a pivotal role in the intricate web of protein-protein interactions. The interaction scores for these genes were calculated using three algorithms within the CytoHubba plug-in: MNC(Fig. 8B), the Degree(Fig. 8C), MCC(Fig. 8D). Then, the top10 genes of the three algorithms were crossed and Venn diagram was drawn (Fig. 8E). A total of 9 hub genes were obtained: IL1A, TSLP, SUZ12, TLR3, DNMT3B, BRD 4, DNMT3A, HSP90AA1 and CDK 9.

3.8. TF- mRNA and mRNA-miRNA interaction networks

We delved into the discovery of the critical TFs that bind to the hub genes. Leveraging the CHIPBase database (version 2.0), we

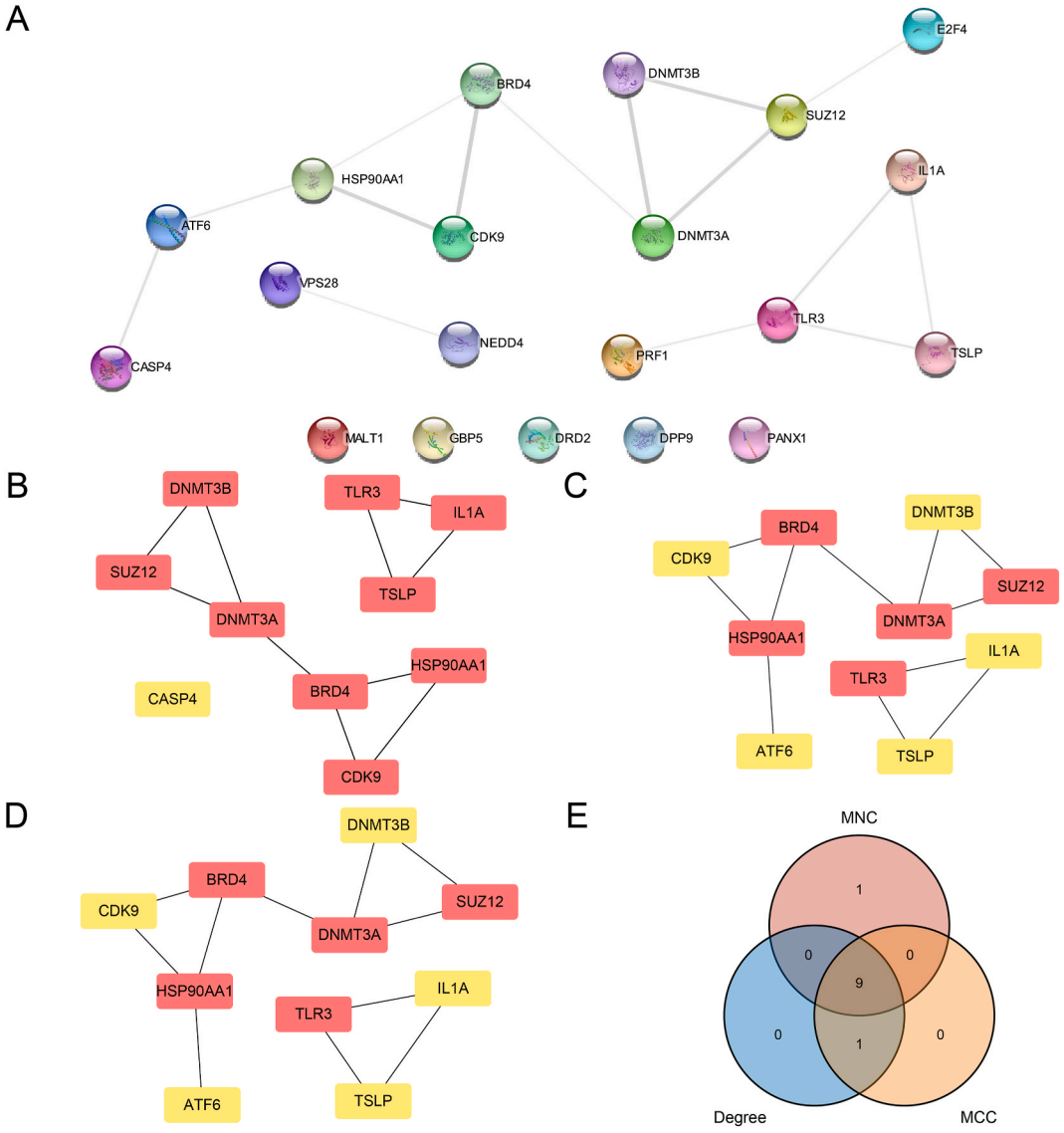

Fig. 8. PPI network and hub genes analysis.
(A) PPI network of the pyroptosis-related LASSO genes. (B) TOP10 pyroptosis-related LASSO genes in MNC algorithm plots PPI Network. (C) TOP10 pyroptosis-related LASSO genes in Degree algorithm plots PPI Network. (D) TOP10 pyroptosis-related LASSO genes in MCC algorithm plots PPI Network. (E) Venn diagram of LASSO gene (LASSO Genes) in TOP10 cells of 3 algorithms. Block color from red to yellow represents scoring from high to low.

were able to identify these essential regulators and subsequently construct a comprehensive TF-mRNA regulatory network(Fig. 9A). Interaction relationship data for 9 genes IL1A, TSLP, SUZ12, TLR3, DNMT3B, BRD4, DNMT3A, HSP90AA1, CDK9 and 91 TFs were obtained.

Upon receiving the miRNA (hub Genes) data from the StarBase database, a comprehensive mRNA-miRNA regulation network was constructed and graphically represented through the utilization of the sophisticated Cytoscape software(Fig. 9B). Our intricate network of mRNA-miRNA interactions contained 88 miRNA molecules and 8 hub genes(IL1A, TSLP, SUZ12, DNMT3B, BRD4, DNMT3A, HSP90AA1, CDK 9).

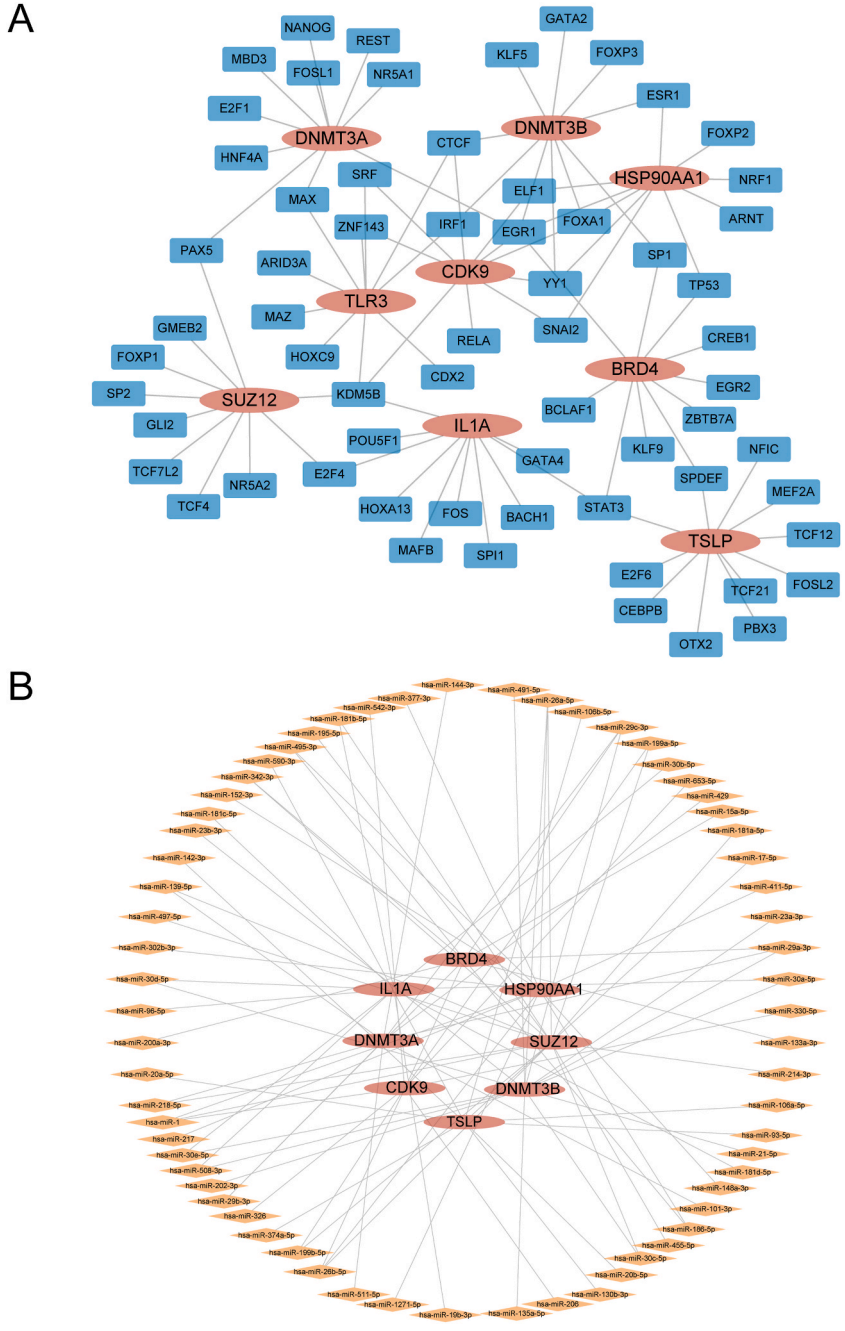

Fig. 9. TF-mRNA and mRNA-miRNA regulatory network.
(A) The TF-mRNA, (B) and the mRNA-miRNA interaction networks of the key genes. The red oval is mRNA, the blue rectangle is TF, and the orange diamond is miRNA.TF: transcription factors.

3.9. Functional enrichment analysis (GO) and pathway enrichment (KEGG) analysis of pyroptosis-related hub genes

To analyze the BP, MF, CC, and pathways related to the 9 pyroptosis-related hub genes in MAFLD, we used GO and KEGG enrichment analysis methodologies(Table 3). Based on the comprehensive findings, the 9 pivotal hub genes in MAFLD were mainly enriched in BP, including covalent chromatin modification, macromolecule methylation, positive regulation of histone modification, phosphorylation of RNA polymerase II C-terminal domain and positive regulation of chromatin organization; CC, including sex chromosome, nuclear heterochromatin, nuclear chromatin, heterochromatin and nuclear cyclin-dependent protein kinase holoenzyme complex and MF, such as RNA polymerase II CTD heptapeptide repeat kinase activity, S-adenosylmethionine-dependent methyltransferase activity, methyltransferase activity, transferase activity and histone deacetylase binding. Meanwhile, it was also enriched in pathways such as Necroptosis, Cysteine and methionine metabolism, Fluid shear stress and atherosclerosis, and InfluenzaA in KEGG enrichment analysis. The outcomes of the GO gene functional enrichment analysis, alongside the KEGG gene functional enrichment analysis, were depicted in a captivating bubble map (Fig. 10A),

Moreover, the intricate GO (Fig. 10B) and KEGG (Fig. 10C) networks were crafted based on the exhaustive functional enrichment analysis of GO and KEGG genes. These linkages delineate the respective molecules and their corresponding annotations, where the size of the node is directly proportional to the abundance of molecules. Subsequently, a comprehensive GO and KEGG enrichment analysis was conducted for the 9 pivotal genes. The z-score for each entry was precisely calculated with logFC values, and was visually represented through bar graphs (Fig. 10D). The outcomes of the GO and KEGG analyses showed that the nuclear chromatin pathway stoods as a potentially prominent positive regulatory route, whereas the histone deacetylase binding pathway appeared to be the most notable negative regulatory path.

3.10. GSEA of differentially expressed genes in MAFLD

To gain a profound understanding of the influence exerted by DEGs levels on the emergence of MAFLD, we delved into the intricate

Table 3
Results of GO and KEGG enrichment analysis.

ONTOLOGY	ID	Description	GeneRatio	BgRatio	pvalue	p.adjust	qvalue
BP	GO:0016569	covalent chromatin modification	5/9	474/18670	1.20E-06	6.21E-04	2.67E-04
BP	GO:0043414	macromolecule methylation	4/9	309/18670	8.68E-06	1.20E-03	5.18E-04
BP	GO:0031058	positive regulation of histone modification	3/9	90/18670	8.91E-06	1.20E-03	5.18E-04
BP	GO:0070816	phosphorylation of RNA polymerase II C-terminal domain	2/9	10/18670	9.28E-06	1.20E-03	5.18E-04
BP	GO:1905269	positive regulation of chromatin organization	3/9	103/18670	1.34E-05	1.34E-03	5.78E-04
CC	GO:0000803	sex chromosome	2/9	30/19717	8.00E-05	3.01E-03	1.50E-03
CC	GO:0005720	nuclear heterochromatin	2/9	35/19717	1.09E-04	3.01E-03	1.50E-03
CC	GO:0000790	nuclear chromatin	3/9	377/19717	5.35E-04	7.51E-03	3.74E-03
CC	GO:0000792	heterochromatin	2/9	78/19717	5.46E-04	7.51E-03	3.74E-03
CC	GO:0019908	nuclear cyclin-dependent protein kinase holoenzyme complex	1/9	12/19717	5.47E-03	4.38E-02	2.18E-02
MF	GO:0008353	RNA polymerase II CTD heptapeptide repeat kinase activity	2/9	18/17697	3.50E-05	1.41E-03	1.68E-04
MF	GO:0008757	S-adenosylmethionine-dependent methyltransferase activity	3/9	155/17697	5.33E-05	1.41E-03	1.68E-04
MF	GO:0008168	methyltransferase activity	3/9	215/17697	1.41E-04	2.16E-03	2.58E-04
MF	GO:0016741	transferase activity, transferring one-carbon groups	3/9	226/17697	1.63E-04	2.16E-03	2.58E-04
MF	GO:0042826	histone deacetylase binding	2/9	111/17697	1.36E-03	1.45E-02	1.72E-03
KEGG	hsa04217	Necroptosis	3/7	159/8076	2.47E-04	1.01E-02	8.59E-03
KEGG	hsa00270	Cysteine and methionine metabolism	2/7	50/8076	7.73E-04	1.59E-02	1.34E-02
KEGG	hsa05418	Fluid shear stress and atherosclerosis	2/7	139/8076	5.84E-03	7.98E-02	6.76E-02
KEGG	hsa05164	Influenza A	2/7	171/8076	8.73E-03	8.95E-02	7.58E-02

GO,Gene Ontology; BP,Biological Process; CC,Cellular Component; MF,Molecular Function; KEGG, Kyoto Encyclopedia of Genes and Genomes.

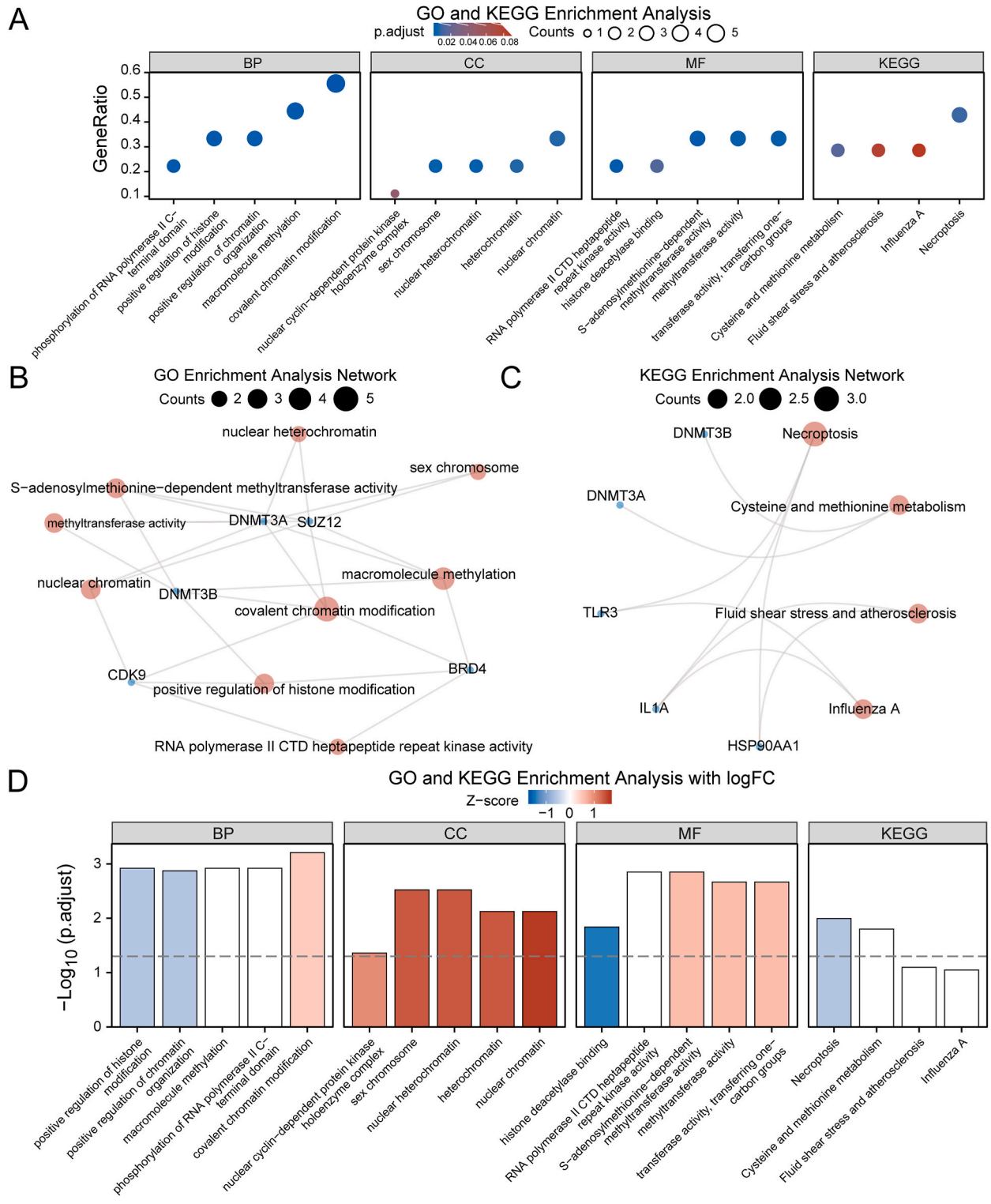

Fig. 10. GO and KEGG Enrichment Analysis for pyroptosis-related hub genes.
(A) Pyroptosis-related hub genes GO function enrichment analysis results displayed as a bubble diagram: biological process, cell component, molecular function, KEGG. (B–C) pyroptosis-related hub genes GO function enrichment (B) KEGG pathway enrichment analysis (C) results displayed as a network diagram. (D) Bar graphs display of the GO function enrichment and KEGG pathway enrichment with combined logFC analysis results for the pyroptosis-related hub genes. The logFC bar graphs (D) red dots stand for genes that have been upregulated (logFC>0) and blue dots for genes that have been downregulated (logFC<0).

relationship between these DEGs and the diverse biological processes they are intertwined with. Additionally, we examined the specific cellular components they impact and the crucial molecular functions they fulfill, all through the lens of a comprehensive GSEA enrichment analysis(Table 4).The result showed the DEGs were significantly enriched in the TNF-A Signaling via NF-KB (Fig. 11B), inflammatory response (Fig. 11C), IL6-JAK-STAT3 Signaling (Fig. 11D), apoptosis(Fig. 11E) and hypoxia (Fig. 11F).

3.11. Immune-infiltration analysis of the MAFLD dataset

The MAFLD datasets were uploaded to the CIBERSORTx online website, and the correlation between the 22 immune cells in the MAFLD group and the Normal group was calculated using the CIBERSORTx algorithm. Drawing from the outcomes of the immune infiltration analysis, the proportion of immune cells in the Combined Datasets bar plot (Fig. 12A) and the group comparison scatter plot (Fig. 12B) were crafted. Notably, the variations in the expression of Mast cells, both in their resting and activated states, exhibit an exceedingly significant distinction among the diverse groups within the MAFLD dataset, attaining a remarkable P value of less than 0.001. Furthermore, the analysis reveals that the expression levels of Monocytes also exhibit a pronounced statistical significance between the varied groups within the MAFLD dataset, marked by a P value below 0.01. Finally, the correlation of three immune cell infiltrates with pyroptosis-related hub genes in the MAFLD datasets was visualized by the lollipop chart (Fig. 12C–E).

3.12. Construction of the related disease subtypes of MAFLD

Utilizing the "ConsensusClusterPlus" package within the R programming language, we analyzed data centered around 9 pivotal genes that are intricately linked to pyroptosis (IL1A, TSLP, SUZ12, TLR3, DNMT3B, BRD4, DNMT3A, HSP90AA1 and CDK9), to investigate the variations in PRDEG expression in MAFLD sample group (group: MAFLD), within the MAFLD sample.To identify the different disease subtypes associated with MAFLD, we used consistent clustering methods. Two MAFLD subtypes (cluster1 and cluster2) were finalized (Fig. 13A–D). MAFLD subtype 1 (cluster1) contained 36 samples, and MAFLD subtype 2 (cluster2) contained 10 samples. The PCA clustering analysis revealed profound disparities among the two distinct disease subtypes, as depicted in Fig. 13D. The comprehensive heatmap showed the diverse expression patterns of nine key pyroptosis-associated hub genes across the two disease subtypes within the MAFLD dataset.(Fig. 13E).

To provide a deeper insight into relationships between the expression of 9 pyroptosis-related hub genes and the MAFLD subtypes (cluster 1 and cluster 2) we have presented the correlation analysis in the form of group comparison plots (Fig. 13F). The result showed that the expression levels of five pivotal genes exhibit statistically notable disparities across the varying MAFLD subtypes, ($P < 0.05$). Remarkably, the expression levels of TLR3 and TSLP genes were highly significant, exhibiting a profound statistical significance in their differential expression between the MAFLD subtypes($P < 0.001$); Similarly, CDK9 and SUZ12 genes also manifest a substantial statistical significance in their expression levels among the diverse MAFLD subtypes ($P < 0.01$); the expression level of gene HSP90AA1 displayed a notable statistical significance in distinguishing the MAFLD subtypes ($P < 0.05$). while, the expression levels of the genes BRD4, DNMT3A, DNMT3B and IL1A did not exhibit any substantial variation between different MAFLD subtypes ($P \geq 0.05$)

Subsequently, we plotted the ROC curves of 5 hub genes (TLR3, TSLP, CDK9, SUZ12, HSP90AA1) in the two MAFLD subtypes and presented the results (Fig. 13G–K). As shown from ROC curves, the hub gene CDK 9 (Fig. 13G, AUC = 0.778), HSP90AA1 (Fig. 13H, AUC = 0.719), SUZ12 (Fig. 13I, AUC = 0.792), TLR3 (Fig. 13J, AUC = 0.844) and the TSLP (Fig. 13K, AUC = 0.844) revealed a distinct correlation among the various subtypes of MAFLD ($0.7 < AUC < 0.9$).

3.13. Analysis of the immune infiltration via ssGSEA based on the two distinct subtypes of MAFLD

We calculated the infiltration abundance of immune cells in two disease subtypes (cluster1, cluster2) for MAFLD group samples in the MAFLD dataset.The group comparison boxplot demonstrated the variation in immune cell infiltration quantity (Fig. 14A).The comprehensive analysis of the MAFLD dataset revealed striking variations in the infiltration abundance of five distinct immune cell types among the diverse MAFLD subtypes ($P < 0.05$). Among them, the expression levels of CD56dim natural killer cell, Neutrophil and Regulatory were highly statistically significant between different MAFLD subtypes($P < 0.01$); the expression levels of Natural killer cell and Natural killer T cell were statistically significant between different MAFLD subtypes ($P < 0.05$). This observation underscores the intricacy and heterogeneity of immune cell infiltration patterns in MAFLD.

Table 4
Results of combined datasets GSEA.

ID	setSize	enrichmentScore	NES	pvalue	p.adjust	qvalues
HALLMARK_TNFA_SIGNALING_VIA_NFKB	189	0.369	1.712	0.000	0.005	0.005
HALLMARK_INFLAMMATORY_RESPONSE	197	0.388	1.809	0.000	0.005	0.005
HALLMARK_COMPLEMENT	182	0.342	1.578	0.000	0.007	0.006
HALLMARK_IL6_JAK_STAT3_SIGNALING	84	0.407	1.657	0.003	0.035	0.031
HALLMARK_APOPTOSIS	158	0.331	1.499	0.004	0.039	0.035
HALLMARK_HYPOXIA	182	0.301	1.392	0.011	0.091	0.081
HALLMARK_REACTIVE_OXYGEN_SPECIES_PATHWAY	44	0.418	1.504	0.025	0.176	0.155
HALLMARK_INTERFERON_GAMMA_RESPONSE	187	0.284	1.317	0.028	0.177	0.157

GSEA, Gene Set Enrichment Analysis。.

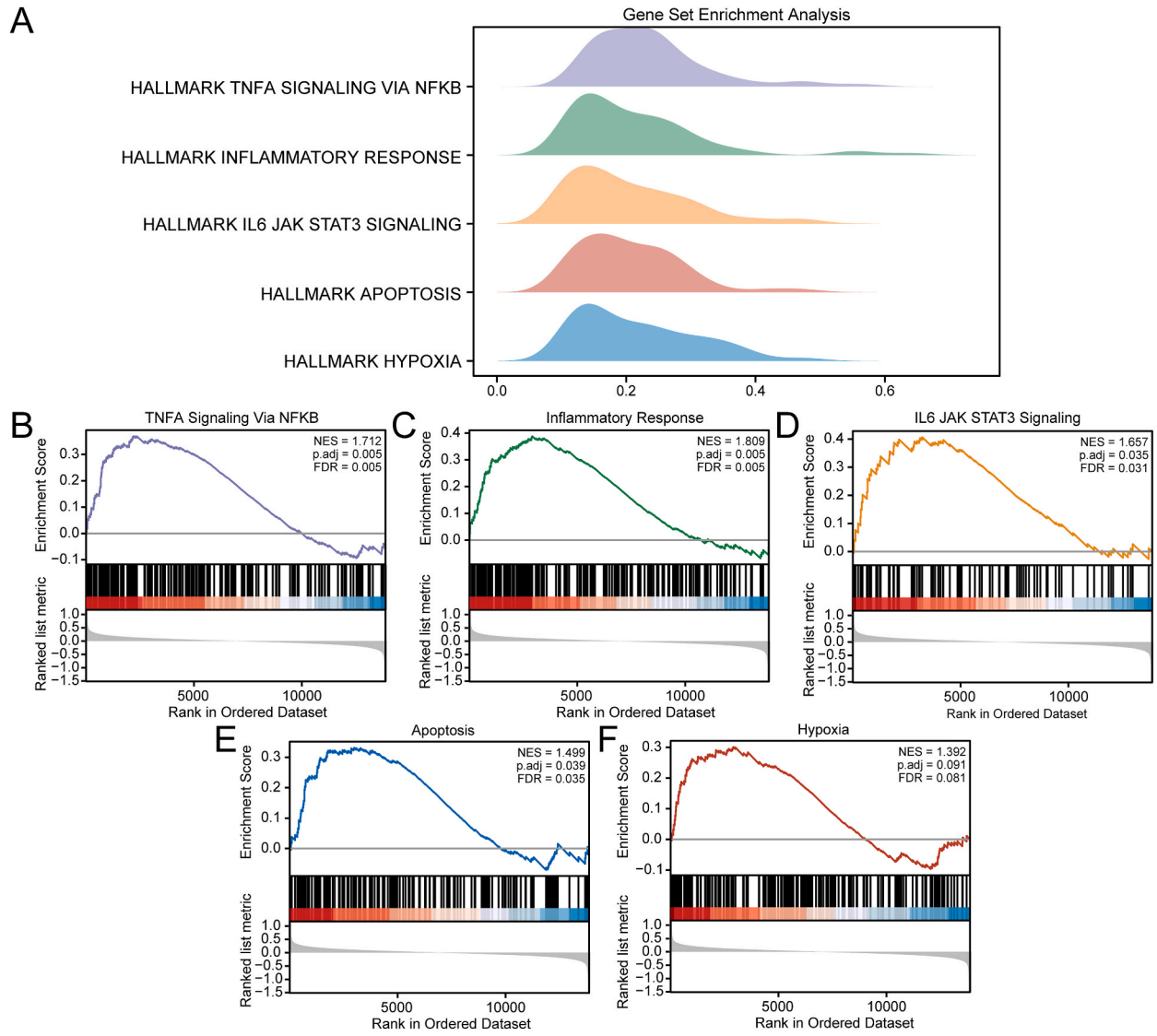

Fig. 11. GSEA for MAFLD datasets.
(A) GSEA analysis of the MAFLD dataset, and 5 biological functions showed by mountain maps. (B–F) In the MAFLD dataset, the differentially expressed genes (DEGs) exhibited a remarkable enrichment in diverse biological pathways. These pathways encompassed (B) TNF-A Signaling via NF-KB signaling, (C) inflammatory response, (D) IL6-JAK-STAT3 Signaling pathway, (E) apoptosis (F)and hypoxia The GSEA's criteria for significant enrichment entailed a statistical significance threshold of $P < 0.05$, along with a stringent False Discovery Rate (FDR) value (q-value) of less than 0.05.

Group comparison plots from the outcomes of the ssGSEA immune infiltration study demonstrated a correlation between the statistically significant abundance of immune cell infiltration in the various MAFLD subtypes(Fig. 14B–C). The results showed that Natural killer cell and Natural killer T cell had the highest association in cluster1 (Fig. 14B) (cor value = 0.49); Natural killer cell and Neutrophil had the highest association in cluster2 (Fig. 14C) (cor value = 0.51). In addition, the correlation between the abundance of 5 immune cell infiltrates and the expression of nine pyroptosis-related hub genes in two disease subtypes was analyzed (Fig. 14D–E) by drawing related heat map. The results showed that in cluster1(Fig. 14D), hub gene HSP90AA1 and Natural killer T cell, DNMT3A and Activated CD4 T cell were significantly negatively correlated; In cluster2 (Fig. 14E), hub gene BRD4 and Natural killer T cell were significantly negatively correlated.

3.14. The evaluation of the expression of potential candidate genes within the MAFLD cellular model

Integrating the aforementioned analysis results, HSP90AA1, TSLP, CDK9, and BRD4 occupy pivotal roles in the immune infiltration process associated with pyroptosis in MAFLD. Utilizing RT-qPCR techniques, we investigated the expression of these genes within a

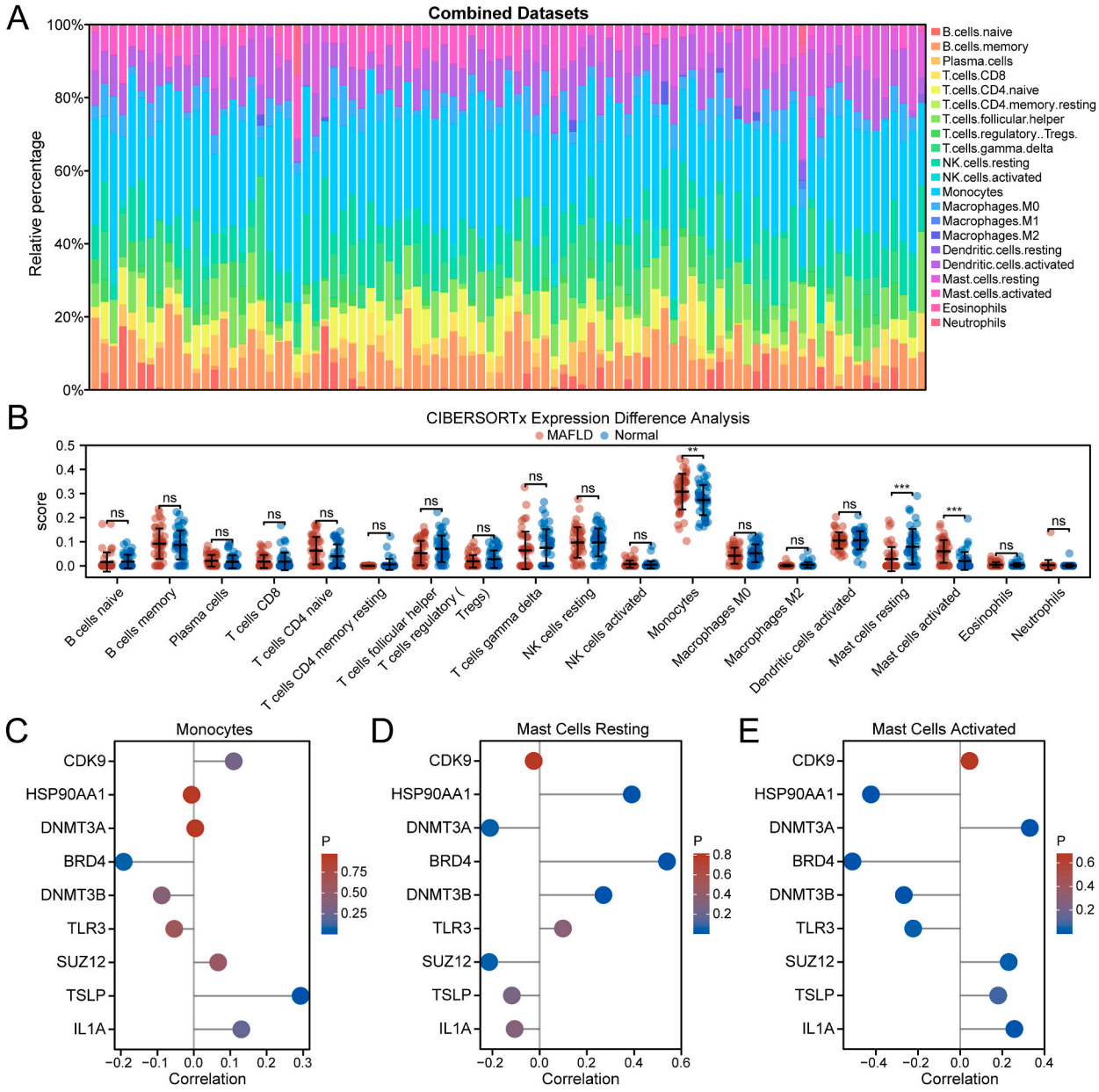

Fig. 12. Comprehensive immune infiltration analysis of MAFLD datasets by CIBERSORTx algorithm.
(A) Histogram of immune cells in the combined datasets. (B) Scatter plot of group comparison of immune cell infiltration abundance in the combined datasets. (C-E) Correlation of pyroptosis-related hub genes with immune cell Monocytes (C), Mast cells resting (D), Mast cells activated (E) infiltration abundance in the combined datasets. MAFLD group is shown in red and the Normal group in blue. The ns represents $P \geq 0.05$, indicating the absence of statistical significance; * * represents $P < 0.01$, highly statistically significant; * * * represents $P < 0.001$, highly statistically significant.

cellular model of MAFLD. The PCR results (Fig. 15) indicated that, in comparison to the control group, the expression levels of four genes were notably elevated in the SHC group and moderately increased in the FLC group. Except for CDK9, the remaining results exhibited statistical significance. Notably, the expression of CDK9 did not demonstrate a statistically significant difference between the FLC group and the control group.

4. Discussion

MAFLD is one of the most prevalent metabolic diseases worldwide, with a prevalence rate as high as 25 %, meaning that one in four people may suffer from MAFLD [2,54]. Increasing evidence suggests that MAFLD is a "multisystem" illness that not only affects the

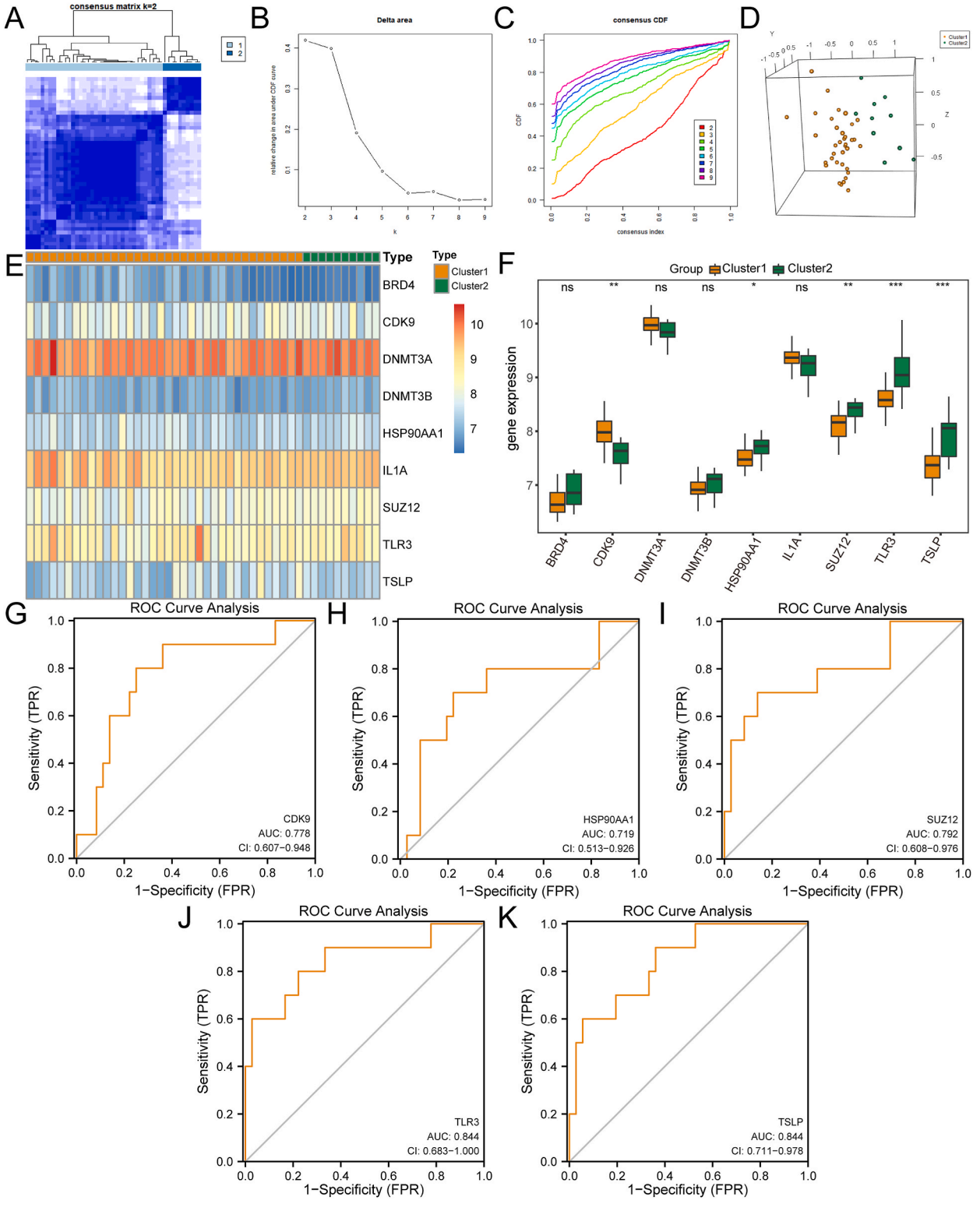

(caption on next page)

Fig. 13. Consensus clustering analysis for hub genes.
(A) A diagram illustrating the consistently clustered outcomes pertaining to MAFLD diseases. (B) Delta plot of different subtypes by consensus cluster analysis. (C) The CDF plot for the consensus cluster analysis. (D) The PCA plots of the two MAFLD subtypes (cluster1 and cluster2). (E) The complex numerical heat map of FRDEGs in two MAFLD subtypes. (F) Group comparison plots of FRDEGs in two MAFLD subtypes. (G–K) The ROC curves of hub genes (G) CDK9, (H) HSP90AA1, (I) SUZ12, (J) TLR3, (K) TSL in two MAFLD subtypes. In the complex numerical heat maps and group comparison plots, orange indicates cluster1 and light green indicates cluster2.

vasculature and other organ systems [55], but also severely damages the liver (resulting in cirrhosis) [56]. The most severe manifestation of steatohepatitis arises from intricate interactions between metabolic and stress pathways within hepatocytes, initiated by chronic and excessive accumulation of fat and inflammatory responses, further escalated by immune cell infiltration [57]. At present, there is a scarcity of medical therapeutic options available for patients suffering from MAFLD.

Pyroptosis is a form of programmed cell death characterized by cell lysis and the release of numerous inflammatory factors (IL-1β, IL-18), which can lead to a severe inflammatory response. By targeting and adjusting the intricate biochemical pathways involved in pyroptosis, we may uncover novel therapeutic strategies Recent years, more and more rearches have revealed that pyroptosis participate in the progression of MAFLD. Therefore, immune infiltration was highly associated with pyroptosis in MAFLD [58,59]. Our comprehensive study rigorously analyzed pyroptosis-related genes employing bioinformatics techniques, subsequently exploring the immunologic features of MAFLD and identifying novel therapeutic targets for future drug development.

Our findings demonstrated a tight connection between the DEGs of MAFLD and genes involved in pyroptosis, identifying 44 PRDEGs. Based on these PRDEGs, we constructed a diagnostic model comprising 20 LASSO genes: BRD4, MALT1, DPP9, SUZ12, TLR3, PRF1, DNMT3B, IL1A, E2F4, VPS28, PANX1, TSLP, DRD2, DNMT3A, ATF6, HSP90AA1, CASP4, CDK9, GBP5 and NEDD4. We successfully created a nomogram to predict the likelihood of developing steatohepatitis, and we used these LASSO genes to identify high-risk and low-risk groups, 10 of them were statistically significant (p value < 0.05). Then we analyzed the immune infiltration in the risk model, 5 immune cells were statistically significant (p value < 0.05): T follicular helper cell(p value < 0.001),Central memory CD8 T cell (p value < 0.01), Activated CD4 T cell,CD56dim natural killer cell and Neutrophil (p value < 0.05). In the related heat map results: in the high risk group (Fig. 7D), the gene DPP9 and CD56dim natural killer cell were clearly positively correlated, the gene HSP90AA1 and CD56dim natural killer cell were significantly negatively associated; in the low risk group (Fig. 7E), the gene TSLP and Neutrophil cell were clearly positively correlated, the gene BRD4 and Central memory CD8 T cel were significantly negatively associated.

Through PPI analysis of the 20 pyroptosis-related LASSO genes, we identified nine hub genes: IL1A, TSLP, SUZ12, TLR3, DNMT3B, BRD4, DNMT3A, HSP90AA1and CDK9. A TF-mRNA regulatory network consisting of 9 hub genes and 91 transcription factors has been constructed. Additionally, we built an mRNA-miRNA regulatory network including eight pyroptosis-related hub genes (IL1A, TSLP, SUZ12, DNMT3B, BRD4, DNMT3A, HSP90AA1, CDK 9) and 88 miRNA molecules.

The results of GO, KEGG analyses of 9 hub genes indicated that the nuclear chromatin pathway stoods as a potentially prominent positive regulatory route, whereas the histone deacetylase binding pathway appeared to be the most notable negative regulatory path. GSEA showed the DEGs in the integrated GEO dataset were significantly affected TNF-A signaling via NF-KB signaling, Inflammatory Response, IL6- JAK-STAT3 signaling, Apoptosis and Hypoxia. This aligns well with numerous previous investigations, which have definitively substantiated the involvement of pyroptosis genes in the progression of MAFLD via these intricate signaling pathways [60–64]. Then, we used CIBERSORTx Online website to analyze the correlations between 22 immune cells and 9 hub genes, the result showed that the correlation between Mast cells activated and gene CDK9 in MAFLD group was the highest.

In our study, we found that the variability of MAFLD is closely associated to genes related to pyroptosis. Consensus clustering using the expression of pyroptosis-associated genes allowed the identification of two subtypes of MAFLD (Cluster1 and Cluster2). To verify the differential expression of 9 hub genes in two subtypes, we found that 5 hub genes (TLR3, TSLP, CDK9, SUZ12, HSP90AA1) were statistically significant (p value < 0.05). In addition to CDK9, the expression levels of other genes were observed to be notably higher in Cluster 2 compared to Cluster 1. This observation may indicate that Cluster 2 potentially represents a "pyroptosis-active" phenotype, whereas Cluster 1 exhibits a "pyroptosis-suppressive" phenotype. Subsequently, we investigated the variations in immune infiltration across different disease subtypes (Cluster 1 and Cluster 2). The results revealed statistically significant differences (p value < 0.05) in the infiltration of five immune cell types: CD56dim natural killer cell, Neutrophil, Regulatory T cell, Natural killer cell, and Natural killer T cell. Remarkably, the infiltration abundance of all immune cell types was significantly elevated in Cluster 2 in comparison to Cluster 1. This finding suggests that Cluster 2 may be characterized as an "immunoactivity" type, whereas Cluster 1 exhibits an "immunosuppressive" phenotype. The correlation between the abundance of 5 immune cell infiltrates and the expression of 9 hub genes in the two disease subtypes showed that gene HSP90AA1 and Natural killer T cell were clearly positively correlated in Cluster1, DNMT3A and Activated CD4 T cell were clearly negatively correlated in Cluster1. While in Cluster2 BRD4 and Natural killer T cell were clearly negatively correlated.

DNMT3A: As an epigenetic regulator, it may affect the function and infiltration of immune cells by regulating DNA methylation. The current studies found that human DNMT3A coordinate mRNA expression in normal tissues and overexpressed in tumors [65]. But were rarely reported in other diseases. Our study analyzed DNMT3A and Activated CD4 T cell were clearly negatively correlated in Cluster1. Maybe DNMT3A took part in the process for MAFLD.

Based on a comprehensive analysis of the available data, we have determined that HSP90AA1, TSLP, CDK9, and BRD4 exert significant influences on pyroptosis-related immune infiltration in MAFLD. Furthermore, through cellular experimental validation (Fig. 15), we observed that the expression levels of these four genes were notably higher in the SHC group compared to the FLC group, indicating an elevated expression in steatohepatitis compared to the pure high-fat model.

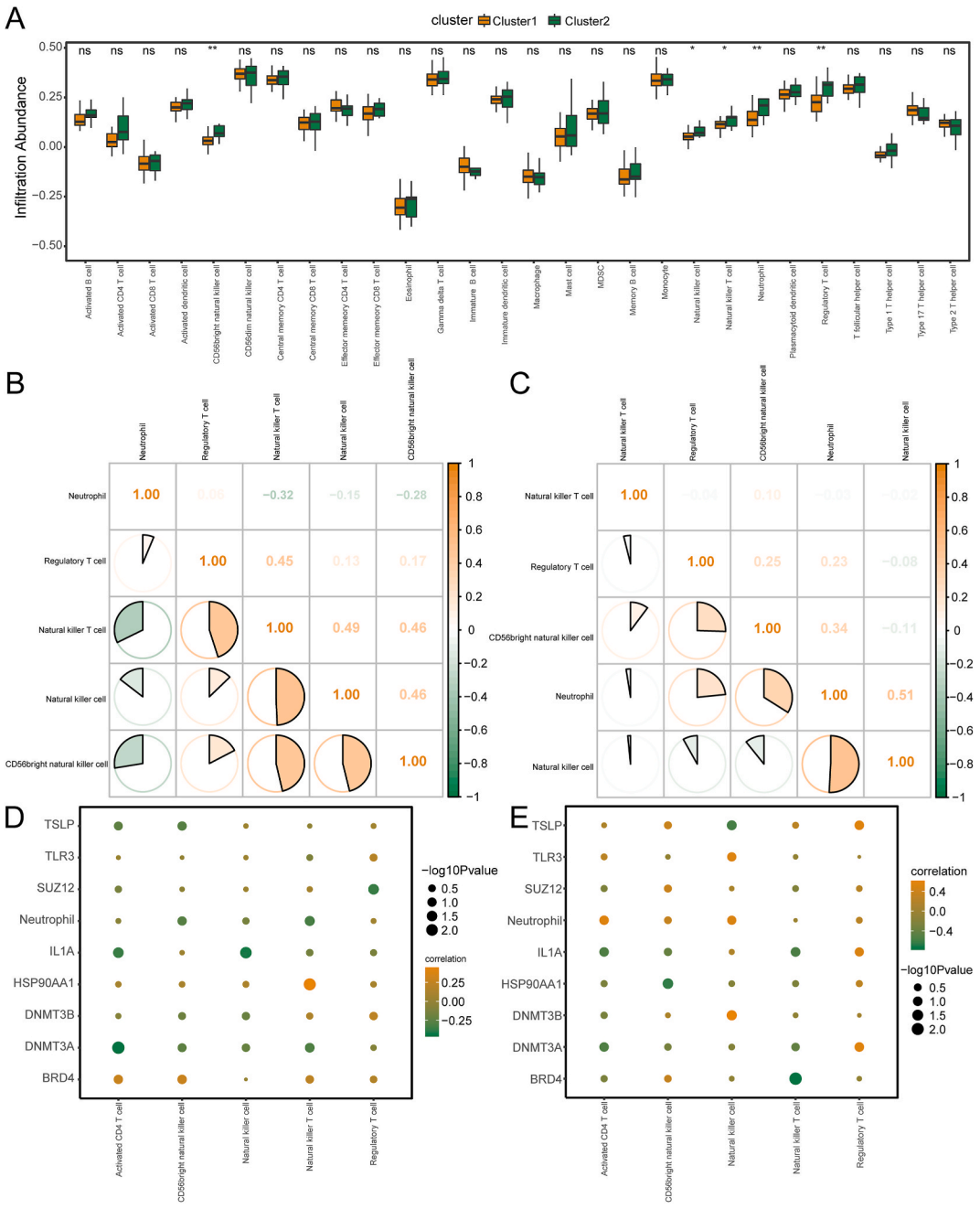

Fig. 14. Cluster Group Immune Infiltration Analysis by ssGSEA Algorithm.
(A) Group comparison of results of ssGSEA immune infiltration analysis between two MAFLD subtypes. (B–C) Results of the correlation analysis of the abundance of 5 immune cell infiltrates in cluster1 (B) and cluster2 (C) are presented. (D–E) Heatmap of the correlation between immune cells and hub genes in the MAFLD subtypes cluster1 (D), cluster2 (E). In A, Cluster1 is shown in orange and Cluster2 in green. The symbol "ns" is analogous to a P-value greater than or equal to 0.05, indicating the absence of statistical significance; conversely, the symbol "*" represents a P-value less than 0.05, thus indicating statistical significance. The double asterisk "**" signifies a P-value less than 0.01, denoting a high level of statistical significance. The triple asterisk "***" corresponds to a P-value less than 0.001, which is also indicative of a profound statistical significance.

HSP90AA1 was one number of the heat shock protein 90 (HSP90s) family and might alter immunological functions such as antigen presentation, lymphocyte activation, and immune infiltration, which are more thoroughly researched in tumor diseases [66]. In addition to this, HSP90AA1 was one of the risk genes for predicting the occurrence of ischemic stroke [67] and was connected to the Braak stages of Alzheimer's disease [68]. While HSP90AA1 has not been extensively studied in MAFLD, The resent research has shown that USP14-HSP90AA1-CYP2E1 axis contributes to NAFLD progression [69], Our study is the first to identify HSP90AA1 as

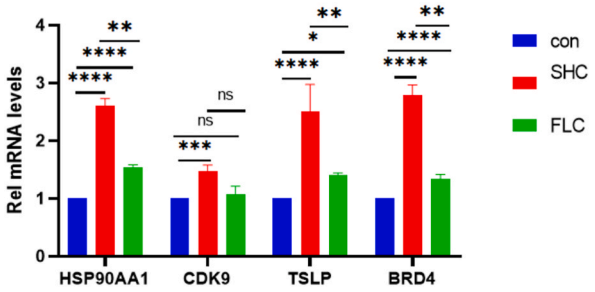

Fig. 15. PCR-method validation of candidate gene expression in MAFLD cell model.
(A) The expression of HSP90AA1, TSLP,CDK9 and BRD4 in cell model of MAFLD. The symbol ns represents $P \geq 0.05$, not statistically significant; the symbol * is comparable to $P < 0.05$, statistically significant; symbol * * is comparable to $P < 0.01$, highly statistically significant; symbol * * * is comparable to $P < 0.001$, highly statistically significant; and symbol * * * * *is comparable to $P < 0.0001$.

pyroptosis-related gene and immune infiltration related gene in MAFLD. Our results showed that the gene HSP90AA1 and CD56dim natural killer cell were significantly negatively associated in the high risk group of MAFLD, and were clearly positively correlated in Cluster1(immunosuppressive type). It has been demonstrated that natural killer cells can prevent liver fibrosis and carcinogenesis, indicating that they may possibly be involved in the pathophysiology of MAFLD. A study pointed out that CD56dim NK cell populations were fewer in MAFLD patients compared with healthy volunteers [70]. Therefore, we infered that HSP90AA1 took part in the process for MAFLD, whose possible molecular mechanism was that increased expression of HSP90AA1 reduced the CD56dim NK cell number, which led to a reduced capacity of resistance to liver fibrosis.

Thymic stromal lymphopoietin (TSLP), a lymphocyte growth factor, was first discovered in a mouse thymic stromal cell line as a pleiotropic cytokine. Activated intestine and lung epithelial cells, keratinocytes, and fibroblasts are the main sources of TSLP expression. It has been found that some immune cells can produce TSLP. Among the potential targets for TSLP are immunological cells [71]. Our study also showed that TSLP and Neutrophil cell were clearly positively correlated. TSLP was first linked to a number of allergic illnesses, including eosinophilic esophagitis, bronchial asthma, and atopic dermatitis. A growing body of research suggests that TSLP contributes to chronic inflammatory conditions including Chronic obstructive pulmonary disease [72]. However, there are few studies on TSLP in MAFLD and the results were inconsistent. One study indicated that TSLP-stimulated T cells promote sebum secretion, which can be pharmacologically manipulated to promote adipose loss, might improve obesity-associated MAFLD [73]. Another study has shown that over expression of miR-142-5p could attenuate MAFLD progression via inhibiting TSLP and JAK-STAT pathway [74]. Our study showed that the expression of TSLP was high in Cluster2(pyroptosis-active type) of MAFLD, However, in the low risk group for MAFLD, it was positively connected with neutrophils, which was inconsistent with other findings.

CDK9 (Cyclin Dependent Kinase 9), a significant transcription-regulating member of the CDK family connected to cell cycling, shows markedly increased activity in numerous cancer forms [75]. In MAFLD, CDK9 expression is also raised. Methyltransferase-like 3 (METTL3) has emerged as a pivotal negative regulatory element in the intricate network that drives the pathogenesis of MAFLD. Notably, its influence is intertwined with the CDK9-mediated phosphorylation mechanism [76]. An in-depth examination has uncovered an intriguing finding: in the presence of MAFLD, the Wilms' tumor 1-associating protein (WTAP) undergoes a significant relocation, shifting from its native position in the nucleus to the cytoplasm, which is also intricately linked to the phosphorylation process mediated by CDK9 [77]. Our study identified CDK9 was one of pyroptosis-related gene in MAFLD, and was highly associated with Mast cells activated. Mast cells exhibit a pivotal role in augmenting hepatic harm, and they potentially contribute to the development of microvascular steatosis during the transition from MAFLD to steatohepatitis [78]. In summary, we induced that maybe CDK9-mediated phosphorylation can activate Mast cells to accelerate the progression from MAFLD progression to steatohepatitis. But this needed to be confirmed in future.

The transcriptional epigenetic regulator, Bromodomain-Containing Protein 4 (BRD4), plays a pivotal role in the evolution and escalation of both inflammatory disorders and malignancies [79]. Extensive research has revealed that BRD4 orchestrates the acetylation-dependent congregation of transcriptional regulator complexes, thus activating a diverse array of transcriptional programs [80,81]. Multiple BET inhibitors are currently undergoing preclinical and clinical trials for the treatment of multiple tumors [79]. According to certain studies, alcohol-associated liver disease (ALD) has a split-new entry through the BRD4-induced inflammatory response [82]. However, there have been no studies of the role of BRD 4 in MAFLD. In our study BRD4 and Central memory CD8 T cell were significantly negatively associated in low risk model. An earlier work found that the transcription factor BATF can be directly controlled by BRD4 in $CD8^+$ T cells, which was linked to the development of T cells into an effector memory state [83]. So BRD4 can regulate Central memory CD8 T cell. While our study also found BRD4 and Natural killer T cell were clearly negatively correlated. Liver NK cells play a pivotal role in the intricate process of MAFLD's development. It could protect against liver fibrosis and tumorigenesis. From our results, we inferred that the increased expression of BRD4 suppresses the numbers of NK cells which led to the weakened inhibitory effect of the latter on liver fibrosis. Perhaps there will be more research on BRD4 in MAFLD.

However, it is worth noting that this research does possess a few inherent limitations First, we used publicly accessible databases, constraining our capacity to incorporate a wider range of demographic and clinical variables into our longitudinal analyses Secondly, the scope of our research was inherently constrained by the datasets that were available to us, specifically focusing on patients suffering from MAFLD. Thirdly, our list of pyroptosis-related genes, though derived from regularly updated databases such as

GeneCards, GSEA, and PubMed, is not exhaustive. It is essential that future research endeavors delve deeper into the mechanisms of pyroptosis in MAFLD, while taking into account the limitations posed by bioinformatics methodologies.

5. Conclusions

We identified 10 hub genes (IL1A, TSLP, SUZ12, TLR3, DNMT3B, BRD4, DNMT3A, HSP90AA1, CDK9 and CASP4) as potential pyroptosis-related biomarkers with utility in disease diagnosis and prognostication. Four of these hub genes (HSP90AA1, TSLP, CDK9 and BRD4) were also correlated with the different immune cells in various grouping models of MAFLD. Consequently, a comprehensive analysis of the pyroptosis-associated genetic signature was undertaken, revealing insightful immunologic features of MAFLD. This may spur innovative therapeutic modalities, encompassing precision-tailored therapies, particularly in the realm of immunotherapy.

Ethics approval and consent to participate

As the article content does not pertain to ethical considerations, the procurement of approval from an ethics committee was deemed unnecessary for this study.

Consent for publication

Not applicable.

Availability of data and materials

The data used to support the findings during this study areavailable in the GEO database, repository the webset is "https://www.ncbi.nlm.nih.gov/geo/". The pyroptosis-related genes from multiple database sources, which were described in detail in the previous text.

Funding

In relation to the current research, no funding was procured or received for the execution of this study.

CRediT authorship contribution statement

Xin Lian: Writing – review & editing, Writing – original draft, Software, Resources, Project administration, Methodology, Formal analysis, Data curation. **Xulei Tang:** Writing – review & editing, Supervision.

Declaration of competing interest

The authors declare that they have no known competing financial interests or personal relationships that could have appeared to influence the work reported in this paper.

Acknowledgments

The First Clinical Medical College of Lanzhou University.

Appendix A. Supplementary data

Supplementary data to this article can be found online at https://doi.org/10.1016/j.heliyon.2024.e34348.

References

[1] M. Eslam, P.N. Newsome, S.K. Sarin, et al., A new definition for metabolic dysfunction-associated fatty liver disease: an international expert consensus statement, J. Hepatol. 73 (1) (2020) 202–209, https://doi.org/10.1016/j.jhep.2020.03.039.
[2] Z. Younossi, Q.M. Anstee, M. Marietti, et al., Global burden of nafld and nash: trends, predictions, risk factors and prevention, Nat. Rev. Gastroenterol. Hepatol. 15 (1) (2018) 11–20, https://doi.org/10.1038/nrgastro.2017.109.
[3] S. Mittal, H.B. El-Serag, Y.H. Sada, et al., Hepatocellular carcinoma in the absence of cirrhosis in United States veterans is associated with nonalcoholic fatty liver disease, Clin. Gastroenterol. Hepatol. 14 (1) (2016) 124–131, https://doi.org/10.1016/j.cgh.2015.07.019.
[4] S. Singh, A.M. Allen, Z. Wang, L.J. Prokop, M.H. Murad, R. Loomba, Fibrosis progression in nonalcoholic fatty liver vs nonalcoholic steatohepatitis: a systematic review and meta-analysis of paired-biopsy studies, Clin. Gastroenterol. Hepatol. 13 (4) (2015) 643–654, https://doi.org/10.1016/j.cgh.2014.04.014. , quiz e39-quiz e40.
[5] L. Vonghia, P. Michielsen, S. Francque, Immunological mechanisms in the pathophysiology of non-alcoholic steatohepatitis, Int. J. Mol. Sci. 14 (10) (2013) 19867–19890, https://doi.org/10.3390/ijms141019867.

[6] E. Liaskou, H.W. Zimmermann, K.K. Li, et al., Monocyte subsets in human liver disease show distinct phenotypic and functional characteristics, Hepatology 57 (1) (2013) 385–398, https://doi.org/10.1002/hep.26016.
[7] M.J. Wolf, A. Adili, K. Piotrowitz, et al., Metabolic activation of intrahepatic cd8+ t cells and nkt cells causes nonalcoholic steatohepatitis and liver cancer via cross-talk with hepatocytes, Cancer Cell 26 (4) (2014) 549–564, https://doi.org/10.1016/j.ccell.2014.09.003.
[8] X. Hildebrandt, M. Ibrahim, N. Peltzer, Cell death and inflammation during obesity: "know my methods, wat(son)", Cell Death Differ. 30 (2) (2023) 279–292, https://doi.org/10.1038/s41418-022-01062-4.
[9] W. Arif, B. Mathur, M.F. Saikali, et al., Splicing factor srsf1 deficiency in the liver triggers nash-like pathology and cell death, Nat. Commun. 14 (1) (2023) 551, https://doi.org/10.1038/s41467-023-35932-3.
[10] T. Mahata, A.S. Sengar, M. Basak, et al., Hepatic regulator of g protein signaling 6 (rgs6) drives non-alcoholic fatty liver disease by promoting oxidative stress and atm-dependent cell death, Redox Biol. 46 (2021) 102105, https://doi.org/10.1016/j.redox.2021.102105.
[11] B.T. Xu, F.Y. Teng, Q. Wu, et al., Bdh1 overexpression ameliorates hepatic injury by activation of nrf2 in a mafld mouse model, Cell Death Dis. 8 (1) (2022) 49, https://doi.org/10.1038/s41420-022-00840-w.
[12] I. Vitale, F. Pietrocola, E. Guilbaud, et al., Apoptotic cell death in disease-current understanding of the nccd 2023, Cell Death Differ. 30 (5) (2023) 1097–1154, https://doi.org/10.1038/s41418-023-01153-w.
[13] S.P. Preston, M.D. Stutz, C.C. Allison, et al., Epigenetic silencing of ripk3 in hepatocytes prevents mlkl-mediated necroptosis from contributing to liver pathologies, Gastroenterology 163 (6) (2022) 1643–1657, https://doi.org/10.1053/j.gastro.2022.08.040.
[14] T. Chen, Y. Meng, Z. Zhou, et al., Gas5 protects against nonalcoholic fatty liver disease via mir-28a-5p/march7/nlrp3 axis-mediated pyroptosis, Cell Death Differ. 30 (7) (2023) 1829–1848, https://doi.org/10.1038/s41418-023-01183-4.
[15] J. Tong, D. Li, H. Meng, et al., Targeting a novel inducible gpx4 alternative isoform to alleviate ferroptosis and treat metabolic-associated fatty liver disease, Acta Pharm. Sin. B 12 (9) (2022) 3650–3666, https://doi.org/10.1016/j.apsb.2022.02.003.
[16] J. Tong, X.T. Lan, Z. Zhang, et al., Ferroptosis inhibitor liproxstatin-1 alleviates metabolic dysfunction-associated fatty liver disease in mice: potential involvement of panoptosis, Acta Pharmacol. Sin. 44 (5) (2023) 1014–1028, https://doi.org/10.1038/s41401-022-01010-5.
[17] J.I. Beier, J.M. Banales, Pyroptosis: an inflammatory link between nafld and nash with potential therapeutic implications, J. Hepatol. 68 (4) (2018) 643–645, https://doi.org/10.1016/j.jhep.2018.01.017.
[18] B. Xu, M. Jiang, Y. Chu, et al., Gasdermin d plays a key role as a pyroptosis executor of non-alcoholic steatohepatitis in humans and mice, J. Hepatol. 68 (4) (2018) 773–782, https://doi.org/10.1016/j.jhep.2017.11.040.
[19] F. Alegre, P. Pelegrin, A.E. Feldstein, Inflammasomes in liver fibrosis, Semin, Liver Dis. 37 (2) (2017) 119–127, https://doi.org/10.1055/s-0037-1601350.
[20] A. Wree, A. Eguchi, M.D. Mcgeough, et al., Nlrp3 inflammasome activation results in hepatocyte pyroptosis, liver inflammation, and fibrosis in mice, Hepatology 59 (3) (2014) 898–910, https://doi.org/10.1002/hep.26592.
[21] E.H. Koh, J.E. Yoon, M.S. Ko, et al., Sphingomyelin synthase 1 mediates hepatocyte pyroptosis to trigger non-alcoholic steatohepatitis, Gut 70 (10) (2021) 1954–1964, https://doi.org/10.1136/gutjnl-2020-322509.
[22] K. Yamanishi, S. Maeda, S. Kuwahara-Otani, et al., Deficiency in interleukin-18 promotes differentiation of brown adipose tissue resulting in fat accumulation despite dyslipidemia, J. Transl. Med. 16 (1) (2018) 314, https://doi.org/10.1186/s12967-018-1684-3.
[23] X.W. Fu, C.Q. Song, Identification and validation of pyroptosis-related gene signature to predict prognosis and reveal immune infiltration in hepatocellular carcinoma, Front. Cell Dev. Biol. 9 (2021) 748039, https://doi.org/10.3389/fcell.2021.748039.
[24] X. Lian, X. Tang, Use of a ferroptosis-related gene signature to construct diagnostic and prognostic models for assessing immune infiltration in metabolic dysfunction-associated fatty liver disease, Front. Cell Dev. Biol. 11 (2023) 1199846, https://doi.org/10.3389/fcell.2023.1199846.
[25] M. Ahrens, O. Ammerpohl, W. von Schonfels, et al., Dna methylation analysis in nonalcoholic fatty liver disease suggests distinct disease-specific and remodeling signatures after bariatric surgery, Cell Metabol. 18 (2) (2013) 296–302, https://doi.org/10.1016/j.cmet.2013.07.004.
[26] I. Frades, E. Andreasson, J.M. Mato, E. Alexandersson, R. Matthiesen, M.L. Martinez-Chantar, Integrative genomic signatures of hepatocellular carcinoma derived from nonalcoholic fatty liver disease, PLoS One 10 (5) (2015) e124544, https://doi.org/10.1371/journal.pone.0124544.
[27] B.M. Arendt, E.M. Comelli, D.W. Ma, et al., Altered hepatic gene expression in nonalcoholic fatty liver disease is associated with lower hepatic n-3 and n-6 polyunsaturated fatty acids, Hepatology 61 (5) (2015) 1565–1578, https://doi.org/10.1002/hep.27695.
[28] S. Davis, P.S. Meltzer, Geoquery: a bridge between the gene expression omnibus (geo) and bioconductor, Bioinformatics 23 (14) (2007) 1846–1847, https://doi.org/10.1093/bioinformatics/btm254.
[29] J.T. Leek, W.E. Johnson, H.S. Parker, A.E. Jaffe, J.D. Storey, The sva package for removing batch effects and other unwanted variation in high-throughput experiments, Bioinformatics 28 (6) (2012) 882–883, https://doi.org/10.1093/bioinformatics/bts034.
[30] G. Stelzer, N. Rosen, I. Plaschkes, et al., The genecards suite: from gene data mining to disease genome sequence analyses, Curr Protoc Bioinformatics 54 (2016) 1–30, https://doi.org/10.1002/cpbi.5.
[31] A. Subramanian, P. Tamayo, V.K. Mootha, et al., Gene set enrichment analysis: a knowledge-based approach for interpreting genome-wide expression profiles, Proc. Natl. Acad. Sci. U.S.A. 102 (43) (2005) 15545–15550, https://doi.org/10.1073/pnas.0506580102.
[32] Y. Ye, Q. Dai, H. Qi, A novel defined pyroptosis-related gene signature for predicting the prognosis of ovarian cancer, Cell Death Dis. 7 (1) (2021) 71, https://doi.org/10.1038/s41420-021-00451-x.
[33] Z. Dong, L. Bian, M. Wang, L. Wang, Y. Wang, Identification of a pyroptosis-related gene signature for prediction of overall survival in lung adenocarcinoma, JAMA Oncol. 2021 (2021) 6365459, https://doi.org/10.1155/2021/6365459.
[34] M.I. Love, W. Huber, S. Anders, Moderated estimation of fold change and dispersion for rna-seq data with deseq2, Genome Biol. 15 (12) (2014) 550, https://doi.org/10.1186/s13059-014-0550-8.
[35] H. Zhang, P. Meltzer, S. Davis, Rcircos: an r package for circos 2d track plots, BMC Bioinf. 14 (2013) 244, https://doi.org/10.1186/1471-2105-14-244.
[36] S.H. Park, J.M. Goo, C.H. Jo, Receiver operating characteristic (roc) curve: practical review for radiologists, Korean J. Radiol. 5 (1) (2004) 11–18, https://doi.org/10.3348/kjr.2004.5.1.11.
[37] S. Engebretsen, J. Bohlin, Statistical predictions with glmnet, Clin. Epigenet. 11 (1) (2019) 123, https://doi.org/10.1186/s13148-019-0730-1.
[38] J. Wu, H. Zhang, L. Li, et al., A nomogram for predicting overall survival in patients with low-grade endometrial stromal sarcoma: a population-based analysis, Cancer Commun. 40 (7) (2020) 301–312, https://doi.org/10.1002/cac2.12067.
[39] B. Van Calster, L. Wynants, J. Verbeek, et al., Reporting and interpreting decision curve analysis: a guide for investigators, Eur. Urol. 74 (6) (2018) 796–804, https://doi.org/10.1016/j.eururo.2018.08.038.
[40] T. Tataranni, C. Piccoli, Dichloroacetate (dca) and cancer: an overview towards clinical applications, Oxidative Med, Cell. Longev 2019 (2019) 8201079, https://doi.org/10.1155/2019/8201079.
[41] B. Xiao, L. Liu, A. Li, et al., Identification and verification of immune-related gene prognostic signature based on ssgsea for osteosarcoma, Front. Oncol. 10 (2020) 607622, https://doi.org/10.3389/fonc.2020.607622.
[42] D. Szklarczyk, A.L. Gable, D. Lyon, et al., String v11: protein-protein association networks with increased coverage, supporting functional discovery in genome-wide experimental datasets, Nucleic Acids Res. 47 (D1) (2019) D607–D613, https://doi.org/10.1093/nar/gky1131.
[43] C.H. Chin, S.H. Chen, H.H. Wu, C.W. Ho, M.T. Ko, C.Y. Lin, Cytohubba: identifying hub objects and sub-networks from complex interactome, BMC Syst. Biol. 8 (Suppl 4) (2014) S11, https://doi.org/10.1186/1752-0509-8-S4-S11. Suppl 4.
[44] X. Yang, Y. Li, R. Lv, H. Qian, X. Chen, C.F. Yang, Study on the multitarget mechanism and key active ingredients of herba siegesbeckiae and volatile oil against rheumatoid arthritis based on network pharmacology, Evid.-based Complement Altern. Med 2019 (2019) 8957245, https://doi.org/10.1155/2019/8957245.
[45] K.R. Zhou, S. Liu, W.J. Sun, et al., Chipbase v2.0: decoding transcriptional regulatory networks of non-coding rnas and protein-coding genes from chip-seq data, Nucleic Acids Res. 45 (D1) (2017) D43–D50, https://doi.org/10.1093/nar/gkw965.
[46] H. Mi, A. Muruganujan, D. Ebert, X. Huang, P.D. Thomas, Panther version 14: more genomes, a new panther go-slim and improvements in enrichment analysis tools, Nucleic Acids Res. 47 (D1) (2019) D419–D426, https://doi.org/10.1093/nar/gky1038.

[47] M. Kanehisa, S. Goto, Kegg: kyoto encyclopedia of genes and genomes, Nucleic Acids Res. 28 (1) (2000) 27–30, https://doi.org/10.1093/nar/28.1.27.
[48] G. Yu, L.G. Wang, Y. Han, Q.Y. He, Clusterprofiler: an r package for comparing biological themes among gene clusters, OMICS 16 (5) (2012) 284–287, https://doi.org/10.1089/omi.2011.0118.
[49] A. Liberzon, A. Subramanian, R. Pinchback, H. Thorvaldsdottir, P. Tamayo, J.P. Mesirov, Molecular signatures database (msigdb) 3.0, Bioinformatics 27 (12) (2011) 1739–1740, https://doi.org/10.1093/bioinformatics/btr260.
[50] N. Rusk, Expanded cibersortx, Nat. Methods 16 (7) (2019) 577, https://doi.org/10.1038/s41592-019-0486-8.
[51] E.F. Lock, D.B. Dunson, Bayesian consensus clustering, Bioinformatics 29 (20) (2013) 2610–2616, https://doi.org/10.1093/bioinformatics/btt425.
[52] M.D. Wilkerson, D.N. Hayes, Consensusclusterplus: a class discovery tool with confidence assessments and item tracking, Bioinformatics 26 (12) (2010) 1572–1573, https://doi.org/10.1093/bioinformatics/btq170.
[53] Y. Wang, C. Chen, J. Chen, et al., Overexpression of nag-1/gdf15 prevents hepatic steatosis through inhibiting oxidative stress-mediated dsdna release and aim2 inflammasome activation, Redox Biol. 52 (2022) 102322, https://doi.org/10.1016/j.redox.2022.102322.
[54] S.K. Sarin, M. Kumar, M. Eslam, et al., Liver diseases in the asia-pacific region: a lancet gastroenterology & hepatology commission, Lancet Gastroenterol. Hepatol. 5 (2) (2020) 167–228, https://doi.org/10.1016/S2468-1253(19)30342-5.
[55] K.I. Zheng, M. Eslam, J. George, M.H. Zheng, When a new definition overhauls perceptions of mafld related cirrhosis care, Hepatobiliary Surg. Nutr. 9 (6) (2020) 801–804, https://doi.org/10.21037/hbsn-20-725.
[56] G. Targher, H. Tilg, C.D. Byrne, Non-alcoholic fatty liver disease: a multisystem disease requiring a multidisciplinary and holistic approach, Lancet Gastroenterol. Hepatol. 6 (7) (2021) 578–588, https://doi.org/10.1016/S2468-1253(21)00020-0.
[57] J.T. Haas, S. Francque, B. Staels, Pathophysiology and mechanisms of nonalcoholic fatty liver disease, Annu. Rev. Physiol. 78 (2016) 181–205, https://doi.org/10.1146/annurev-physiol-021115-105331.
[58] T. Csak, M. Ganz, J. Pespisa, K. Kodys, A. Dolganiuc, G. Szabo, Fatty acid and endotoxin activate inflammasomes in mouse hepatocytes that release danger signals to stimulate immune cells, Hepatology 54 (1) (2011) 133–144, https://doi.org/10.1002/hep.24341.
[59] M. Ganz, G. Szabo, Immune and inflammatory pathways in nash, Hepatol. Int. 7 (Suppl 2) (2013) 771–781, https://doi.org/10.1007/s12072-013-9468-6. Suppl 2.
[60] S. Ezquerro, F. Mocha, G. Fruhbeck, et al., Ghrelin reduces tnf-alpha-induced human hepatocyte apoptosis, autophagy, and pyroptosis: role in obesity-associated nafld, J. Clin. Endocrinol. Metab. 104 (1) (2019) 21–37, https://doi.org/10.1210/jc.2018-01171.
[61] Y. Yao, C. Li, F. Qian, et al., Ginsenoside rg1 inhibits microglia pyroptosis induced by lipopolysaccharide through regulating stat3 signaling, J. Inflamm. Res. 14 (2021) 6619–6632, https://doi.org/10.2147/JIR.S326888.
[62] W. Yang, K. Tao, P. Zhang, X. Chen, X. Sun, R. Li, Maresin 1 protects against lipopolysaccharide/d-galactosamine-induced acute liver injury by inhibiting macrophage pyroptosis and inflammatory response, Biochem. Pharmacol. 195 (2022) 114863, https://doi.org/10.1016/j.bcp.2021.114863.
[63] K. Kadono, S. Kageyama, K. Nakamura, et al., Myeloid ikaros-sirt1 signaling axis regulates hepatic inflammation and pyroptosis in ischemia-stressed mouse and human liver, J. Hepatol. 76 (4) (2022) 896–909, https://doi.org/10.1016/j.jhep.2021.11.026.
[64] S. Hua, M. Ma, X. Fei, Y. Zhang, F. Gong, M. Fang, Glycyrrhizin attenuates hepatic ischemia-reperfusion injury by suppressing hmgb1-dependent gsdmd-mediated kupffer cells pyroptosis, Int. Immunopharm. 68 (2019) 145–155, https://doi.org/10.1016/j.intimp.2019.01.002.
[65] K.D. Robertson, E. Uzvolgyi, G. Liang, et al., The human dna methyltransferases (dnmts) 1, 3a and 3b: coordinate mrna expression in normal tissues and overexpression in tumors, Nucleic Acids Res. 27 (11) (1999) 2291–2298, https://doi.org/10.1093/nar/27.11.2291.
[66] D.A. Proia, G.F. Kaufmann, Targeting heat-shock protein 90 (hsp90) as a complementary strategy to immune checkpoint blockade for cancer therapy, Cancer Immunol. Res. 3 (6) (2015) 583–589, https://doi.org/10.1158/2326-6066.CIR-15-0057.
[67] J. Cai, Z. Ye, Y. Hu, et al., Identification of immunogenic cell death-related gene classification patterns and immune infiltration characterization in ischemic stroke based on machine learning, Front. Cell. Neurosci. 16 (2022) 1094500, https://doi.org/10.3389/fncel.2022.1094500.
[68] X.H. Qian, X.L. Liu, S.D. Chen, H.D. Tang, Identification of immune hub genes associated with braak stages in alzheimer's disease and their correlation of immune infiltration, Front. Aging Neurosci. 14 (2022) 887168, https://doi.org/10.3389/fnagi.2022.887168.
[69] D. Wei, X. Tian, L. Zhu, H. Wang, C. Sun, Usp14 governs cyp2e1 to promote nonalcoholic fatty liver disease through deubiquitination and stabilization of hsp90aa1, Cell Death Dis. 14 (8) (2023) 566, https://doi.org/10.1038/s41419-023-06091-6.
[70] Y. Sakamoto, S. Yoshio, H. Doi, et al., Increased frequency of dysfunctional siglec-7(-)cd57(+)pd-1(+) natural killer cells in patients with non-alcoholic fatty liver disease, Front. Immunol. 12 (2021) 603133, https://doi.org/10.3389/fimmu.2021.603133.
[71] G. Varricchi, A. Pecoraro, G. Marone, et al., Thymic stromal lymphopoietin isoforms, inflammatory disorders, and cancer, Front. Immunol. 9 (2018) 1595, https://doi.org/10.3389/fimmu.2018.01595.
[72] S. Ying, B. O'Connor, J. Ratoff, et al., Expression and cellular provenance of thymic stromal lymphopoietin and chemokines in patients with severe asthma and chronic obstructive pulmonary disease, J. Immunol. 181 (4) (2008) 2790–2798, https://doi.org/10.4049/jimmunol.181.4.2790.
[73] R. Choa, J. Tohyama, S. Wada, et al., Thymic stromal lymphopoietin induces adipose loss through sebum hypersecretion, Science 373 (6554) (2021), https://doi.org/10.1126/science.abd2893.
[74] C. Zhou, P. Wang, L. Lei, Y. Huang, Y. Wu, Overexpression of mir-142-5p inhibits the progression of nonalcoholic steatohepatitis by targeting tslp and inhibiting jak-stat signaling pathway, Aging (Albany NY) 12 (10) (2020) 9066–9084, https://doi.org/10.18632/aging.103172.
[75] R. Mandal, S. Becker, K. Strebhardt, Targeting cdk9 for anti-cancer therapeutics, Cancers 13 (9) (2021), https://doi.org/10.3390/cancers13092181.
[76] X. Li, B. Yuan, M. Lu, et al., The methyltransferase mettl3 negatively regulates nonalcoholic steatohepatitis (nash) progression, Nat. Commun. 12 (1) (2021) 7213, https://doi.org/10.1038/s41467-021-27539-3.
[77] X. Li, K. Ding, X. Li, et al., Deficiency of wtap in hepatocytes induces lipoatrophy and non-alcoholic steatohepatitis (nash), Nat. Commun. 13 (1) (2022) 4549, https://doi.org/10.1038/s41467-022-32163-w.
[78] L. Kennedy, V. Meadows, A. Sybenga, et al., Mast cells promote nonalcoholic fatty liver disease phenotypes and microvesicular steatosis in mice fed a western diet, Hepatology 74 (1) (2021) 164–182, https://doi.org/10.1002/hep.31713.
[79] P. Filippakopoulos, S. Knapp, Targeting bromodomains: epigenetic readers of lysine acetylation, Nat. Rev. Drug Discov. 13 (5) (2014) 337–356, https://doi.org/10.1038/nrd4286.
[80] A. Dey, A. Nishiyama, T. Karpova, J. Mcnally, K. Ozato, Brd4 marks select genes on mitotic chromatin and directs postmitotic transcription, Mol. Biol. Cell 20 (23) (2009) 4899–4909, https://doi.org/10.1091/mbc.e09-05-0380.
[81] T. Maruyama, A. Farina, A. Dey, et al., A mammalian bromodomain protein, brd4, interacts with replication factor c and inhibits progression to s phase, Mol. Cell Biol. 22 (18) (2002) 6509–6520, https://doi.org/10.1128/MCB.22.18.6509-6520.2002.
[82] J. Chu, R. Yan, S. Wang, et al., Sinapic acid reduces oxidative stress and pyroptosis via inhibition of brd4 in alcoholic liver disease, Front. Pharmacol. 12 (2021) 668708, https://doi.org/10.3389/fphar.2021.668708.
[83] Y. Kagoya, M. Nakatsugawa, Y. Yamashita, et al., Bet bromodomain inhibition enhances t cell persistence and function in adoptive immunotherapy models, J. Clin. Invest. 126 (9) (2016) 3479–3494, https://doi.org/10.1172/JCI86437.